Title: Shallow slow slip events along the Nankai Trough detected by the GNSS-A

Authors: Yusuke Yokota[1]*, Tadashi Ishikawa[2]*.

Affiliations:

[1] Institute of Industrial Science, University of Tokyo, 4-6-1, Komaba, Meguro-ku, Tokyo 153-8505, Japan.

[2] Hydrographic and Oceanographic Department, Japan Coast Guard, 3-1-1, Kasumigaseki, Chiyoda-ku, Tokyo 100-8932, Japan.

*Correspondence authors: Y. Yokota (yyokota@iis.u-tokyo.ac.jp) or T. Ishikawa (ishikawa@jodc.go.jp).

Abstract: Various slow earthquakes (SEQs), including tremors, very-low-frequency events, and slow slip events (SSEs), occur along megathrust zones. In a shallow plate boundary region, although many SEQs have been observed along pan-Pacific subduction zones, SSEs with a duration on the order of a year or with a large slip have not yet been detected due to difficulty in offshore observation. We try to statistically detect transient seafloor crustal deformations from seafloor geodetic data obtained by the Global Navigation Satellite System-Acoustic combination technique (GNSS-A), which enables monitoring the seafloor absolute position. Here, we report the first detection of signals probably caused by shallow large SSEs along the Nankai Trough and indicate the timings and approximate locations of probable SSEs. The results show the existence of large SSEs around the shallow side of strong coupling regions and indicate the spatiotemporal relationship with other SEQ activities expected in past studies.

One Sentence Summary: Slow slip events discovered around the shallow side of coupling regions have a spatiotemporal relationship with other slow earthquakes.

INTRODUCTION: In the last two decades, many kinds of slow earthquakes (SEQs), including aseismic slow slip events (SSEs), have been detected using onshore high-precision seismometers and Global Navigation Satellite System (GNSS) networks (*1-4*). Along the Nankai Trough in western Japan, where recurring interplate megathrust earthquakes have occurred (*5, 6*) and which has a dense seismic and geodetic monitoring network, their interrelationships have been discussed and compared in detail (*4, 7-10*). Most SEQs occurred not in a strong coupling region, but rather around such a region and have features of repeatedly occurring and migrating. Different types of SEQs sequentially occurred in the neighboring region, and temporal synchronization with other SEQs was also observed.

Observation of deep and shallow SEQ analogies and differences has multidisciplinary value with respect to the physical process of the plate boundary, submarine geology, and earthquake disaster research. However, shallow SEQs cannot be easily monitored due to the technological difficulty of observation in the offshore region. With recent advances in technology, shallow SEQs, such as tremors, very-low frequency events (VLFs), and short-term SSEs with durations on the order of days, have been detected by high-precision onshore seismometers, seafloor seismometers, ocean bottom pressure gauges, and subseafloor borehole strainmeters (*11-15*). However, only SSEs with durations on the order of a year or with a large slip have not yet been detected in the group of shallow SEQs. From the analogy of deep SSEs, GNSS-like geodetic observation is necessary in order to detect shallow SSEs.

A seafloor geodetic monitoring technique called the GNSS-Acoustic combination technique (GNSS-A) was proposed in the 1980s and has been developed over the latest two decades (fig. S1). The GNSS-A seafloor geodetic observation greatly constrained the interplate coupling condition (*16, 17*) along the Nankai Trough subduction zone and detected in detail postseismic fields along the Japan Trench (*18, 19*). Recently, we improved GNSS-A technology and upgraded the observation sensitivity (*20*) in order to detect a transient crustal deformation caused by large interplate slip. Then, GNSS-A monitoring can reveal the occurrence of SSEs which cannot be observed by the onshore geodetic network (fig. S2). The GNSS-A methodology is described in the Materials and Methods section.

RESULTS:

GNSS-A time series and SSE signal detection

We show SSE signals detected in the GNSS-A dataset in Figs. 1 through 5. Our data are listed in data file S1. Signal detection was carried out in the procedure shown in fig. S3. Coseismic and postseismic effects resulting from the 2011 Tohoku-oki earthquake were preliminarily deducted as similar to those described in (*16*) (fig. S4). In order to detect transient events caused by SSEs, we use the concept for the systematic search for SSEs based on the Akaike Information Criterion (AIC) proposed in (*21*). The details of this process are described in the Materials and Methods section. If there was no transient event, the time series can be simply approximated by a straight line. When there is a temporal change due to SSEs in the time series, the time series can be approximated by a piece-wise line. Since the GNSS-A sampling rate is low, it is difficult to estimate the start and end timing of a transient event with sufficient accuracy. Therefore, we did not estimate the duration of transient events in order to prevent overfitting. We set the deformation slope of the piece-wise line to one year out of convenience for detecting a transient event, rather than to indicate that the timescale of an event is one year. The significance of fitting by the piece-wise line to the straight line is verified using the c-AIC (*22, 23*), which is defined as follows:

$$\text{c-AIC} = n\ln(2\pi) + n\ln\left(\frac{RSS}{n}\right) + \frac{2nk}{n-k-1} \quad (1)$$

where n, k, and RSS are the numbers of data, a model parameter, and the residual sum of squares, respectively. If the difference of c-AIC for both lines is negative, the piece-wise line better explains the time series. By estimating this piece-wise line, the timing and scale of transient deformation were determined. We conducted this process for the time series of each site while changing the direction in 10° increments in order to roughly determine the deformation direction. After removing a detected deformation signal, we carried out the same process once again to find out if there was another event. When the difference (Δc-AIC) between c-AICs for the straight line and the piece-wise line is greater than a conveniently determined threshold, the process terminated because there was no clear signal.

We verified this method by applying the method to pseudo datasets. We synthesized the pseudo GNSS-A data and performed the detection process for this pseudo dataset. Detailed settings and results are described in the Materials and Methods section and fig. S6. Considering results in fig. S6, B and C, we set the threshold of Δc-AIC for detecting an SSE signal in order to discuss only deformations of 5 cm or more since a deformation of 4 cm or less is relatively likely to be an error. In the present paper, a threshold is -10. The results in fig. S6D suggest that it is possible to estimate the timing and scale of the event regardless of the length of the slope timescale used for detection. However, the event timescale cannot be determined precisely. In the present paper, only the central time of the event is described.

Detected signals

The time series of seafloor positions and Δc-AICs and the detected deformations are shown along with the time series of the neighbor VLF activity (*11*) in Figs. 1 through 5. At some sites, transient events are detected in 2011-13, as shown in fig. S5. Although the Tohoku-oki earthquake effects were preliminarily deducted by model calculation, the effects are thought to remain in the time series and are detected by Δc-AIC process. Since SSE detection is so difficult in this period, this period is not discussed in the present paper. Detected deformation vectors other than the Tohoku-oki effects are judged as SSE signals and are shown in Figs. 1 through 5.

The reason why all detected deformations are 5 cm or more is due to the sensitivity of the data. There may be smaller cases. Moreover, events with a long timescale cannot currently be detected due to the shortness of the data period. Although the detected cases are considered to be SSEs with durations on the order of a year because of their large deformations, the present low-frequency observation cannot disprove that these were due to small-scale short-term SSE superposition or large-scale short-term SSE.

As shown in Figs. 1 through 5, SSE signals were detected at offshore sites of the Bungo and Kii deep SSEs (*24, 25*). Off the Bungo Channel, signals were detected around 2015-17. Off the Kii Channel, signals were detected around 2008-09 and 2017-18. In addition, SSE signals at sites around Kumano-nada were detected around 2015 and 2017-18. A clear signal was not obtained for the offshore regions of the Tosa Bay and Enshu-nada region.

The time series of nearby GNSS sites (GEONET) are also drawn (*26, 27*). The reference frame for Figs. 1 through 5 is International Terrestrial Reference Frame 2005 (ITRF2005) (*28*). Although the accuracy of GEONET time series varies depending on the installation environment and weather conditions, a displacement of approximately 5 to 7 mm in the horizontal direction is considered to be the detection limit (*29*) in most cases. In the present paper, we set 5 mm as the detection limit. From the GNSS time series, a deformation of more than 5 mm synchronized with the seafloor sites was not clearly visible in all regions, but might have overlapped with other event signals (from earthquakes or deep SSEs).

In the 2017-18 Kii case where two deformation vectors were observed in the same period, we estimated a fault model when it was assumed to be due to single SSE. We discuss timing, approximate location, and minimum magnitude scale of SSE by estimating a rectangular fault model that can explain the detected signals by the grid search method. Here, since there was no clear deformation signal at coastal GEONET sites in this period, we estimated a case of 0 cm (5 mm or less) in the onshore GNSS deformations. In other cases, there was no sufficient data to estimate the fault model, but we verified whether the data can be explained by the slip around each seafloor site by the same analysis. Details of the grid search method and the results are described in the Materials and Methods section and are shown in fig. S7. Shallow VLF activity is also shown in Figs. 1 through 6 (*11*). In the Kii Channel region, detailed shallow VLF source reanalysis for a part of the catalog was also performed considering the 3D structure (*30*). The results are shown in Fig. 3.

A: Bungo Channel region

In a deep region around the Bungo Channel, SSEs repeatedly occurred (*24, 31*). The most recent SSEs occurred intermittently between 2013 and 2016, as shown in the coastal GNSS data (Fig. 1). In addition, as shown in these data, the 2016 Kumamoto earthquake signals were also detected, although this effect was believed to be quite small for seafloor sites. The seafloor signals were detected around the VLF activity region off the Bungo Channel.

The onshore GNSS signals have been interpreted as being due to deep SSEs (*24*). The seafloor signals can be explained by a SSE at depth near sites (1) and (3) or a deeper SSE, according to the estimation shown in fig. S7. According to the seafloor results, the slip area could be extended to a shallower area that was predicted in previous studies (*24*). Since site (4) is far from land area, the signal of site (4) cannot be explained by a deep SSE and suggests the existence of a shallow SSE.

B: Tosa Bay region

In a deep region of the Tosa Bay, many slow earthquakes and short-term SSEs occurred (*10*). On the other hand, a strong coupling condition was estimated in the plate boundary off the Tosa Bay region (*16, 17*). Through our SSE detection process, there was no clear signal at site (5) or (6) (Fig. 2). There was also no clear SSE signal in the nearby GNSS time series except for the Bungo and Kii deep SSEs (*24, 25*).

C: Kii Channel region

Off the Kii Channel, two events were detected around 2008-09 and 2017-18. An SSE of least M_w 6.6 was estimated around 2017-18 according to the grid search results when it was assumed to be due to single SSE (Fig. 3). We did not estimate a fault model of the 2008-09 event, because the signal was detected at only one site. No clear signal was detected at the onshore GNSS sites in these periods. Therefore, the slip region of these two events might be limited to the shallow area.

Since the slip-deficit rate in these shallow regions was calculated as 1 to 3 cm/year (*16, 17*), the 2017-18 Kii SSE was believed to release approximately 10- to 40-year coupling accumulations. However, because of the low station density, the estimation accuracy of the slip-deficit rate is low.

The Kii VLFs were strongly activated in 2009 and 2018 (Fig. 3, A and A''). Although there was activity in 2015, this activity was smaller than the other two cases (Fig. 3A'). The VLF activity in 2009 was slightly closer to the western side than in 2018. The 2008-09 SSE signal was also detected only at site (8) in the western part of the 2017-18 SSE region, although spreading to the west cannot be sufficiently constrained, because there was no western site before 2011. This consistency suggests temporal synchronization and spatial correlation between the SSE and VLF activity in this region. Since the magnitude of the SSE cannot be estimated correctly, the correlation of the activity scales cannot be discussed.

The direction of the signal at site (7) in 2014 was not from south to east and was assumed to be due to deep SSE activity (*25*), which is detected by GNSS, or error. A grid search method was not performed for this signal.

D: Kumano-nada region

The SSE signals off Kumano-nada were detected in the vicinity of short-term SSE activity (*14*) (Fig. 4). In addition, on Apr. 1, 2016, the off-Mie earthquake (M_w 5.6) occurred below this region (*33*). The detected signal might be affected by a short-term SSE and this earthquake. It cannot be distinguished whether it was due to long-term SSE, short-term SSE, or earthquake.

There were also SSE signals around 2016 in the nearby GNSS time series, and these signals were interpreted as being due to deep short-term SSEs just below the Kii Peninsula (*34-36*).

Based on this consideration, the seafloor signals were thought to be only due to the shallow SSEs (fig. S7). However, the onshore signals may be the same source as the signal detected at the seafloor sites. According to the estimation when the onshore signals were due to a shallow source, as shown in fig. S7, F' and G', it is also possible to interpret these signals as being due to shallow SSEs. These signals cannot be clearly identified in the present networks.

Since there was no clear signal in the GEONET sites located at the tip of the Kii Peninsula, it is unlikely that the two events off the Kii Channel and off the Kumano-nada around 2017-18 are connected at a depth just below the seafloor sites. For example, as shown in fig. S7E'', a rectangular SSE model cannot explain the onshore data adequately. However, there is a possibility that the slip regions are connected at an extremely shallow region. This is only true in the case of a smaller slip than the observation limit in the considered networks.

E: Enshu-nada region

In a deeper side of the Enshu-nada region, SSEs recursively occurred (*37*). In a shallower side, a strong coupling condition was estimated in the plate boundary off the Enshu-nada region (*16, 17*). Through our SSE detection process, there was no clear signal at site (13), (14), or (15) (Fig. 5), although there were also deep SSE signals before 2016 in the nearby GNSS time series. This is considered to be due to the short observation period.

DISCUSSION:

The above results and consideration indicate that there were slip regions at least around seafloor sites below the shallow undersea interplate boundary. Fig. 6A shows some slow events detected in other observation networks, the coupling condition, and seafloor site locations. It also highlights the sites at which the signals were detected.

Deep SSEs have a feature such that they occur on the deep side adjacent to a strong coupling region and a historical slip region (*24, 25, 37*). Our results also suggest that the shallow Kii and Kumano-nada SSE signals were detected near the shallow side adjacent to a strong coupling region. The shallow part of the Bungo Channel is also adjacent to the southwest of a shallow strong coupling region. These results indicate the possibility that the edge areas of a coupling region may have two periods that accumulate coupling and release at least a part of the coupling by a deep SSE or a shallow SSE. Our results also directly suggest that non-steady stress occurs in the edge areas of a coupling region in the interseismic period.

Each seafloor SSE signal has a temporal relationship with nearby VLF activity, as shown in Fig. 6B. The signals of sites (1) and (3) were detected simultaneously with VLF activity. The Bungo VLF activity in 2015 shifted to the east, as shown in Fig. 6B. In 2016, the activity was thought to jump across around site (4). The activities of these VLFs and SSEs were roughly synchronized in time.

The Kii VLFs were strongly activated in 2009 and 2018 (Fig. 6B). The signals of sites (8), (9), and (11) were detected in advance and had temporal synchronization and spatial correlation with the shallow VLF activity.

In the Kumano-nada region, VLF activity occurred in 2009 and 2016. Since our dataset did not have enough data before 2009, it is difficult to decide whether the SSE occurred in 2009. The VLF activity in 2016 was monitored around the area between sites (10) and (11) and was associated with short-term SSEs (*15*). Signals were detected both before and after this VLF activity.

Differences in the features of the event occurrences in three regions (Bungo, Kii, and Kumano-nada) may reflect the friction conditions around the coupling region and may also be related to the earthquake history. The friction condition in the shallow Bungo SSE region can be considered not to spread the megathrust event from the east side to the southwest side. The friction condition in shallow Kii SSE region can also be believed as controlling whether the Tonankai earthquake (eastern side of the Kii Peninsula) can spread to the Nankai earthquake (western side) area.

SSE migration and periodicity in the interseismic period were also predicted in earthquake cycle simulations (*38, 39*). Revealing the detailed friction condition and relationship to a megathrust event by future continuous GNSS-A observation will be essential for concrete earthquake simulation of this area. Shallow SSE monitoring will also help promote research on probabilistic earthquake forecasts and earthquake triggering (*40*).

Off the Tosa Bay region and the Enshu-nada region, no clear SSE signal was detected, although these sites may not yet have adequate resolution. The regions off the Tosa Bay and off the Tokai deep SSE are locations where strong coupling regions (*16, 17*) overlapped the assumed and historical seismogenic zones (*5, 6*). The absence of SSEs in our observation period supports the possibility that these regions are the main slip regions of the Nankai Trough megathrust zone.

MATERIALS AND METHODS

Seafloor geodetic observation

Seafloor movements are determined by combining the GNSS observation above the sea and the acoustic ranging system under the sea. This method is called the GNSS-A, which is a unique approach to monitor the absolute horizontal movement directly above the offshore interplate boundary. This technique was proposed in the 1980s (*41*) and was established after the 1990s. We have been developing observation techniques (*42-44*) and have provided valuable data for geodesy and seismology, e.g., the pre-, co-, and post-seismic seafloor crustal deformations of the 2011 Tohoku-oki earthquake (*45-47*) and the interseismic coupling condition along the Nankai Trough (*16*).

A schematic diagram of the seafloor geodetic observation system is shown in Fig. S1. Before 2015, the observation frequency was approximately two to three times/year. After 2016, the acoustic system has been improved in order to observe each site four to 10 times/year (*48, 49*). The details of the GNSS-A system and the data are described in (*50*). The dataset used in the present study was improved from the published data with respect to the underwater sound speed structure error using the method of (*20*).

SSE observation sensitivity of the GNSS-A

Detection capability for SSEs was verified based on the method proposed in (*29*). We verified whether crustal deformations calculated using the SSE fault models set on the plate boundary are observable in the onshore and seafloor geodetic monitoring networks. We assumed crustal deformations for the horizontal component in all of the sites using Green's functions calculated using the formulation of (*51*) considering a homogeneous elastic half-space. The fault models were set considering the magnitude in increments of 0.1 and were deployed every 0.1° on the plate boundary model (*52, 53*), in which dip angles of parts shallower than 10 km were set to roughly match the seismic survey results in (*54*). The fault

size of each magnitude was set according to the scaling law used in (*29*), assuming a rigidity of 10 GPa (smaller than the deep side). This value works only for magnitude in this estimation, but has no effect on the estimation of the slip region or value. The strike angle of the fault model was set to 249° in most areas and was adjusted in areas in which the trough axis angle was largely different. The rake angle was set to 90°.

The root mean squares (RMSs) of the GNSS and GNSS-A data are approximately 3 mm (*29*) and approximately 2 cm or more (*50*), respectively. In the present study, considering these observation abilities, it is judged that SSEs can be detected when the horizontal movements in the onshore and seafloor networks exceed 5 mm and 5 cm, respectively, which are approximately double the RMSs even at one site. Fig. S2, A and B show the resultant maps calculated using the onshore network only and using both the onshore and seafloor networks, respectively. Fig. S2C indicates the SSEs that can be detected only by the seafloor network. These results show that the seafloor network can detect M_w-6-class shallow SSEs that cannot be detected using only the onshore network.

SSE signal detection process using Δc-AIC

We detected an SSE signal according to the process flow shown in Fig. S3. Before the signal detection process, the same deductions as (*16*) on effects resulting from the 2011 Tohoku-oki earthquake were performed for the dataset. Coseismic and postseismic effects were calculated based on the models established in (*55-57*). The resultant time series of their locations at sites along the Nankai Trough are listed in fig. S4 and data file S1. The reference frame is ITRF2005 (*28*).

We detected an SSE signal in these time series based on the method of (*21*) using c-AIC (*22, 23*). We fitted straight and piece-wise lines for the time series and compared each c-AIC to determine whether a time series contains an SSE-like transient deformation. We changed the direction of the time series in 10° increments to extract the maximum deformation angle. The deformation duration of the piece-wise line was set to one year.

This piece-wise line was fitted for the time series data for all periods. The residual sums of squares (RSSs) in Eq. (1) were calculated for the straight and piece-wise lines for the data for the whole periods. The deformation scale was unknown parameter, and a model parameter of the piece-wise line is one more than the straight line. The start timing of deformation was estimated every 0.2 years, and was chosen to minimize c-AIC. We defined Δc-AIC as the difference between c-AICs for the straight line and the piece-wise line.

When a deformation signal of Δc-AIC smaller than a threshold was detected by the piece-wise line, after removing this detected deformation, the same process was performed. When a signal of Δc-AIC smaller than a threshold was not detected, the process ended because there was no clear signal. The threshold was determined by the pseudo data verification described later herein. Signals detected between 2011 and Dec. 2013 were considered to be a remaining influence due to the 2011 Tohoku-oki earthquake, even after the deduction process. In particular, at the sites east of MRT2, the data were strongly affected. Events in this period cannot be identified in the GNSS-A data. In the present paper, we identified a signal only other than this type of signal as an SSE signal. Fig. S5 shows the progression of this process.

The detection limit of this method and the present data were verified using analysis of pseudo data. Fig. S6A shows a pseudo GNSS-A data example of 6 years synthesized considering the present observation ability (1-σ = 2.0 cm, 4 times/year) when a deformation of 5 cm occurs

within 1 year. With this method, 1,000 examples of pseudo data were synthesized for each deformation step. The above detection process was applied to each dataset.

Fig. S6, B and C, show the results for each pseudo dataset. In fig. S6B, the variation in results for each deformation dataset is indicated by the box and whisker plot. For example, the interquartile range for 1-cm deformation data has a spread of approximately ±5 cm. For deformation data of 4 cm or more, the estimation accuracy is stabilized, though a deformation is estimated to be approximately 1 cm smaller on average. Fig. S6C shows the variation of the event timing estimation results. In the case of 5 cm or more, the accuracy is stabilized. These tests suggest that the present data have stable accuracy for deformation steps of 5 cm or more only. In the present paper, we discussed the signal detected when the Δc-AIC threshold for detecting an SSE signal was -10 in order to discuss only deformations of 5 cm or more because a deformation of 4 cm or less is relatively likely to be an error.

Next, the above method was applied to 1,000 examples of pseudo data of 0-, 1-, and 2-year deformation timescales (5-cm deformation step). The deformation steps of the model function were also set to 0, 1, and 2 years, and were applied for three datasets. Fig. S6D shows the variation of the event central time estimation results. The plots show the results obtained by applying the models in which the deformation timescale is 0 (orange), 1 (green), and 2 years (red) to the pseudo data when the deformation timescale is 0 (left), 1 (center), and 2 years (right). The results suggest that, although the event central time can be properly estimated for any timescale event, there is no timescale resolution. Therefore, in the present paper, we do not discuss the event timescale, but rather use the 1-year timescale model to detect only the event central time.

Grid search process to estimate SSE region and regions that could have slips

The 2017-18 Kii SSE fault model can be estimated using a grid search technique, when the deformation fields determined were assumed to be due to single SSE. We set rectangular fault models for a grid every 0.1° on the plate boundary to estimate the weighted RMSEs for the data in the region delimited. The strike angle was set to 249°. The fault length, width, slip, and rake angles were properly changed every 10 km between 20 and 100 km, every 10 km between 20 and 50 km in the dip direction, every 4 cm between 2 and 78 cm, and every 10° between 70° and 130°, respectively. The dip angle was set along the plate boundary model described in the above section (SSE observation sensitivity of the GNSS-A). Crustal deformations were also calculated using the method and setting described in the above section. We calculated crustal deformations for the horizontal component at seafloor sites and the neighbor onshore GNSS sites of the GEONET. Considering the observation abilities, the weighted RMSE was calculated by multiplying the onshore data by nine times the weight of the seafloor data.

Crustal deformation fields detected by GEONET on the coastal region along the Nankai Trough also suggested that there was no deformation field over 5 mm in the time periods of the signals detected at seafloor sites other than deformations discussed in past studies (*24, 25, 31, 34-36*). Figs 1 through 5 show the deformation fields of the 2016 Kumamoto earthquake, the 2013-16 deep intermittent SSE in the Bungo Channel, the 2014-16 deep SSE in the Kii Channel, the 2016 deep short-term SSE in the Kumano-nada region, and the 2013-16 deep SSE in the Enshu-nada region.

Although an SSE model cannot be constructed for other one-site seafloor deformation data, we verified whether the data can be explained by the slip around each seafloor site. The same

analyses as mentioned above were performed for cases other than the 2017-18 Kii Channel case in order to estimate the approximate range of regions that could have slips.

We estimated a case of 0 cm (5 mm or less) in the onshore GNSS deformations (fig. S7, A through G). The distributions of SSE model centers with weighted RMSEs calculated in the range between the minimum and 4 mm greater than the minimum were drawn as regions that could have slips. In the 2017-18 Kii Channel case, the best SSE model and observed and calculated deformation values are compared in fig. S7E. Since small RMSE regions spread in the vicinity of the trough axis, where there is no site, it is difficult to determine the slip region near the trench axis.

Although the onshore GNSS data in Figs. 1 through 5 show a certain degree of appropriateness of the interpretations in past studies (*24, 25, 31, 34-36*), the possibility that, for example, a signal of approximately 5 mm to 1 cm from the shallow source was mixed cannot be clearly rejected. Then, we also estimated cases for a 1-cm onshore southward crustal deformation (other than case C for site (4)). The weighted RMSE distributions are shown in fig. S7, A' through G'.

Signals off the Bungo Channel in 2015-16 (sites (1) and (3)) were synchronized and it is considered that they were due to single SSE sequence, similar to the 2017-18 Kii Channel case (sites (8) and (9)). It is possible to estimate the slip that explains these signals collectively, as shown in fig. S7A'', though RMSEs are larger. As shown in fig. S7, A' and A'', in the northern case off the Bungo Channel, seafloor data can be explained as an effect from a deeper SSE (between the onshore regions and seafloor sites). On the other hand, in other cases, seafloor data cannot be explained by deeper sources.

The data at sites (8), (9), and (10) might have been from the same undersea source. Fig. S7E'' shows an SSE model and the weighted RMSE distribution when trying to estimate sites (8), (9), and (10) collectively. In this case, in which slips occur at similar depths to seafloor sites, it is necessary to cause deformations of approximately 1.7 cm at the onshore GNSS site at the tip of the Kii Peninsula. In reality, no clear signal of 1 cm or more can be seen in the GEONET sites in this period. Therefore, it is thought that there is no slip, at least at this depth.

SUPPLEMENTARY MATERIALS

Fig. S1
Fig. S2
Fig. S3
Fig. S4
Fig. S5
Fig. S6
Fig. S7
Data S1

References and Notes:

1. H. Dragert, K. Wang, T. S. James, A silent slip event on the deeper Cascadia subduction interface. *Science* **292**, 5521, 1525-1528 (2001). doi:10.1126/science.1060152
2. K. Obara, Nonvolcanic deep tremor associated with subduction in southwest Japan. *Science* **296**, 5573, 1679-1681 (2002). doi:10.1126/science.1070378

3. S. Ozawa, M. Murakami, M. Kaidzu, T. Tada, T. Sagiya, Y. Hatanaka, H. Yarai, T. Nishimura, Detection and Monitoring of Ongoing Aseismic Slip in the Tokai Region, Central Japan. *Science* **298**, 5595, 1009-1012 (2002). doi:10.1126/science.1076780
4. H. Hirose, Y. Asano, K. Obara, T. Kimura, T. Matsuzawa, S. Tanaka, T. Maeda, Slow earthquakes linked along dip in the Nankai subduction zone. *Science* **330**, 1502 (2010). doi:10.1126/science.1197102
5. M. Ando, Source mechanism and tectonic significance of historical earthquakes along the Nankai Trough, Japan. *Tectonophysics* **27**, 119-140 (1975). doi:10.1016/0040-1951(75)90102-X
6. T. Sagiya, W. Thatcher, Coseismic slip resolution along a plate boundary megathrust: The Nankai Trough, southwest Japan. *J. Geophys. Res.* **104**, B1, 1111-1129 (1999). doi:10.1029/98JB02644
7. G. Rogers, H. Dragert, Episodic tremor and slip on the Cascadia subduction zone: The chatter of silent slip. *Science* **300**, 5627, 1942-1943 (2003). doi:10.1126/science.1084783
8. S. Ide, G. C. Beroza, D. R. Shelly, T. Uchide, A scaling law for slow earthquakes. *Nature* **447**, 76-79 (2007). doi:10.1038/nature05780
9. S. Ruiz, M. Metois, A. Fuenzalida, J. Ruiz, F. Leyton, R. Grandin, C. Vigny, R. Madariaga, J. Campos, Intense foreshocks and a slow slip event preceded the 2014 Iquique M_w 8.1 earthquake. *Science* **345**, 6201, 1165-1169 (2014) doi:10.1126/science.1256074
10. K. Obara, A. Kato, Connecting slow earthquakes to huge earthquakes. *Science* **353**, 6296, 253-257 (2016). doi:10.1126/science.aaf1512
11. Y. Asano, K. Obara, Y. Ito, Spatiotemporal distribution of very-low frequency earthquakes in Tokachi-oki near the junction of the Kuril and Japan trenches revealed by using array signal processing. *Earth Planet. Space* **60**, 871-875 (2008). doi:10.1186/BF03352839
12. Y. Yamashita, H. Yakiwara, Y. Asano, H. Shimizu, K. Uchida, S. Hirano, K. Umakoshi, H. Miyamachi, M. Nakamoto, M. Fukui, M. Kamizono, H. Kanehara, T. Yamada, M. Shinohara, K. Obara, Migrating tremor off southern Kyushu as evidence for slow slip of a shallow subduction interface. *Science* **348**, 6235, 676-679 (2015). doi:10.1126/science.aaa4242
13. L. M. Wallace, S. C. Webb, Y. Ito, K. Mochizuki, R. Hino, S. Henrys, S. Y. Schwartz, A. F. Sheehan, Slow slip near the trench at the Hikurangi subduction zone, New Zealand. *Science* **352**, 701-704 (2016). doi:10.1126/science.aaf2349
14. E. Araki, D. M. Saffer, A. J. Kopf, L. M. Wallace, T. Kimura, Y. Machida, S. Ide, E. Davis, IODP Expedition 365 shipboard scientists, Recurring and triggered slow-slip events near the trench at the Nankai Trough subduction megathrust. *Science* **356**, 1157-1160 (2017). doi:10.1126/science.aan3120
15. M. Nakano, T. Hori, E. Araki, S. Kodaira, S. Ide, Shallow very-low-frequency earthquakes accompany slow slip events in the Nankai subduction zone. *Nature Comm.* **9**, 984 (2018). doi:10.1038/s41467-018-03431-5
16. Y. Yokota, T. Ishikawa, S. Watanabe, T. Tashiro, A. Asada, Seafloor geodetic constraint for interplate coupling along the Nankai Trough megathrust zone. *Nature* **534**, 374-377 (2016). doi:10.1038/nature17632
17. T. Nishimura, Y. Yokota, K. Tadokoro, T. Ochi, Strain partitioning and interplate coupling along the northern margin of the Philippine Sea plate, estimated from Global Navigation Satellite System and Global Positioning System-Acoustic data. *Geosphere* **14**, 2 (2018). doi:10.1130/GES01529.1

18. F. Tomita, M. Kido, Y. Ohta, T. Iinuma, R. Hino, Along-trench variation in seafloor displacements after the 2011 Tohoku earthquake, *Sci. Adv.* **3**(7), e1700113, doi:10.1126/sciadv.1700113.
19. C. Honsho, M. Kido, F. Tomita, N. Uchida, Offshore postseismic deformation of the 2011 Tohoku earthquake of the 2011 Tohoku earthquake revisited: Application of an improved GPS-acoustic positioning method considering horizontal gradient of sound speed structure, *J. Geophys. Res. Solid Earth* **124**, doi:10.1029/2018JB017135 (2018).
20. Y. Yokota, T. Ishikawa, S. Watanabe, Gradient field of undersea sound speed structure extracted from the GNSS-A oceanography. *Mar. Geophys. Res.* 10.1007/s11001-018-9362-7 (2018).
21. T. Nishimura, T. Matsuzawa, K. Obara, Detection of short-term slow slip events along the Nankai Trough, southwest Japan, using GNSS data. *J. Geophys. Res. Solid Earth* **118**, 3112-3125 (2013). doi:10.1002/jgrb.50222
22. H. Akaike, A new look at the statistical model identification. *IEEE Trans. Auto. Control* **19**, 716-723 (1974). doi:10.1109/TAC.1974.1100705
23. N. Sugiura, Further analysts of the data by Akaike's information criterion and the finite corrections. *Communications in Statics – Theory and Methods* **7,** 1, 13-26 (1976). doi:10.1080/03610927808827599
24. S. Ozawa, Long-term slow slip events along the Nankai trough subduction zone after the 2011 Tohoku earthquake in Japan. *Earth Planet. Space* **69**, 56 (2017). doi:10.1186/s40623-017-0640-4
25. A. Kobayashi, Objective detection of long-term slow slip events along the Nankai Trough using GNSS data (1996-2016). *Earth Planet. Space* **69**, 171 (2017). doi:10.1186/s40623-017-0755-7
26. T. Sagiya, S. Miyazaki, T. Tada, Continuous GPS array and present-day crustal deformation of Japan. *Pure Appl. Geophys.* **157**, 2303-2322 (2000). doi:10.1007/PL00022507
27. H. Nakagawa, et al., Development and validation of GEONET new analysis strategy (Version 4), *J. Geograph. Surv. Inst.*, **118**, 1-8.
28. Z. Altamimi, X. Collilieux, J. Legrand, B. Garayt, C. Boucher, ITRF2005: a new release of the International Terrestrial Reference Frame based on time series of station positions and Earth Orientation Parameters. *Geophys. J. Int.* **112**, B09401 (2007). doi:10.1029/2007JB004949
29. H. Suito, Detectability of interplate fault slip around Japan, based on GEONET daily solution F3. *Journal of Geod. Soc. Japan* **62**, 3, 109-120 (2016).
30. S. Takemura, T. Matsuzawa, A. Noda, T. Tonegawa, Y. Asano, T. Kimura, K. Shiomi, Structural characteristics of the Nankai Trough shallow plate boundary inferred from shallow very low-frequency earthquakes. *Geophys. Res. Lett.* 10.1029/2019GL082448 (2019).
31. S. Ozawa, H. Suito, T. Imakiire, M. Murakmi, Spatiotemporal evolution of aseismic interplate slip between 1996 and 1998 and between 2002 and 2004, in Bungo channel, southwest Japan. *J. Geophys. Res.* **112**, B05409 (2007). doi:10.1029/2006JB004643
32. R. Takagi, N. Uchida, K. Obara, Along-strike variation and migration of long-term slow slip events in the western Nankai subduction zone, Japan. *J. Geophys. Res.* 10.1029/2018JB016738 (2019).
33. S. Takemura, T. Kimura, T. Saito, H. Kubo, K. Shiomi, Moment tensor inversion of the 2016 southeast offshore Mie earthquake in the Tonankai region using a three-dimensional velocity structure model: effects of the accretionary prism and subducting oceanic plate. *Earth Planet. Space* 10.1186/s40623-018-0819-3 (2018).

34. T. Ochi, et al., Short-term slow slip events in the Tokai area, the Kii Peninsula and the Shikoku District, Japan (from May 2016 to October 2016), *Report of the Coordinating Committee for Earthquake Prediction*, **97**, 242-253.
35. T. Ochi, et al., Short-term slow slip events in the Tokai area, the Kii Peninsula and the Shikoku District, Japan (from November 2016 to April 2017), *Report of the Coordinating Committee for Earthquake Prediction*, **98**, 263-274.
36. Geospatial Information Authority of Japan, Crustal movements in the Kinki District, *Report of the Coordinating Committee for Earthquake Prediction*, **100**, 208-218.
37. S. Ozawa, M. Tobita, H. Yarai, A possible restart of an interplate slow slip adjacent to the Tokai seismic gap in Japan. *Earth Planet. Space* **68**, 54 (2016). doi:10.1186/s40623-016-0430-4
38. J. Jiang, N. Lapsta, Connecting depth limits of interseismic locking, microseismicity, and large earthquakes in models of long-term fault slip. *J. Geophys. Res. Solid Earth* **122**, 6491-6523 (2017). doi:10.1002/2017JB014030
39. C. Cattania, P. Segall, Crack models of repeating earthquakes predict observed moment-recurrence scaling. *J. Geophys. Res. Solid Earth* **124**, 476-503 (2019). doi:10.1029/2018JB016056
40. N. Uchida, T. Iinuma, R. M. Nadeau, R. Burgmann, R. Hino, Periodic slow slip triggers megathrust zone earthquakes in northeastern Japan. *Science* **351**, 488-492 (2016). doi:10.1126/science.aad3108
41. F. N. Spiess, Suboceanic geodetic measurements. *IEEE Trans. Geosci. Remote Sensing* **GE-23**, 502-510 (1985).
42. A. Asada, T. Yabuki, Centimeter-level positioning on the seafloor. *Proc. Jpn Acad. Ser. B* **77**, 7-12 (2001).
43. M. Fujita, T. Ishikawa, M. Mochizuki, M. Sato, S. Toyama, M. Katayama, K. Kawai, Y. Matsumoto, T. Yabuki, A. Asada, O. L. Colombo, GPS/acoustic seafloor geodetic observation: method of data analysis and its application. *Earth Planet. Space* **58**, 265-275 (2006). doi:10.1007/s00190-013-0649-9
44. T. Ishikawa, Y. Yokota, Detection of seafloor movement in subduction zones around Japan using a GNSS-A seafloor geodetic observation system from 2013 to 2016. *J. Disaster Res.* **13**, 3, 511-517 (2018). doi:10.20965/jdr.2018.p0511
45. M. Sato, T. Ishikawa, N. Ujihara, S. Yoshida, M. Fujita, M. Mochizuki, A. Asada, Displacement above the hypocenter of the 2011 Tohoku-oki earthquake. *Science* **332**, 1395 (2011). doi:10.1126/science.1207401
46. M. Sato, M. Fujita, Y. Matsumoto, T. Ishikawa, H. Saito, M. Mochizuki, A. Asada, Interplate coupling off northeastern Japan before the 2011 Tohoku-oki earthquake, inferred from seafloor geodetic data. *J. Geophys. Res.* **118**, 1-10 (2013). doi:10.1002/jgrb.50275
47. S. Watanabe, M. Sato, M. Fujita, T. Ishikawa, Y. Yokota, N. Ujihara, A. Asada, Evidence of viscoelastic deformation following the 2011 Tohoku-oki earthquake revealed from seafloor geodetic observation. *Geophys. Res. Lett.* **41**, 5789-5796 (2014). doi:10.1002/2014GL061134
48. Y. Yokota, T. Tashiro, H. Shimomura, Implementation of multi-acoustic ranging system. *Rep. Hydro. Ocean Res.* **55**, 32-37 (2017).
49. M. Matsushita, M. Koike, Improving efficiency in seafloor geodetic observation system using a multi-acoustic ranging method. *Rep. Hydro. Ocean Res.* **56**, 46-49 (2018).
50. Y. Yokota, T. Ishikawa, S. Watanabe, Seafloor crustal deformation data along the subduction zones around Japan obtained by GNSS-A observations. *Scientific Data* **5**, 180182 (2018). doi:10.1038/sdata.2018.182

51. Y. Okada, Internal deformation due to shear and tensile faults in a half-space. *Bull. Seis. Soc. Am.* **82**, 2, 1018-1040 (1992).
52. T. Iwasaki, H. Sato, M. Shinohara, T. Ishiyama, A. Hashima, Fundamental structure model of island arcs and subducted plates in and around Japan. *2015 Fall Meeting, American Geophys. Union, San Francisco*, T31B-2878, 14-18 December 2015.
53. K. G. Lindquist, K. Engle, D. Stahlke, E. Price, Global Topography and Bathymetry Grid Improves Research Efforts. *Eos Trans. AGU*, **85**, 19, 186 (2004). http://onlinelibrary.wiley.com/doi/10.1029/2004EO190003/abstract
54. G. Kimura, Y. Kitamura, Y. Hashimoto, A. Yamaguchi, T. Shibata, K. Ujiie, S. Okamoto, Transition of accretionary wedge structures around the up-dip limit of the seismogenic subduction zone. *Earth Planet. Sci. Lett.* **255**, 471-484 (2007). doi:10.1016/j.epsl.2007.01.005
55. T. Iinuma, R. Hino, M. Kido, D. Inazu, Y. Osada, Y. Ito, M. Ohzono, H. Tsushima, S. Suzuki, H. Fujimoto, S. Miura, Coseismic slip distribution of the 2011 off the Pacific Coast of Tohoku Earthquake (M9.0) refined by means of seafloor geodetic data. *J. Geophys. Res.* **117**, B07409 (2012). doi:10.1029/2012JB009186
56. T. Sun, K. Wang, T. Iinuma, R. Hino, J. He, H. Fujimoto, M. Kido, Y. Osada, S. Miura, Y. Ohta, Y. Hu, Prevalence of viscoelastic relaxation after the 2011 Tohoku-oki earthquake. *Nature* **514**, 84-87 (2014). doi:10.1038/nature13778
57. T. Sun, K. Wang, Viscoelastic relaxation following subduction earthquakes and its effects on afterslip determination. *J. Geophys. Res.* **120**, 1329-1344 (2015). doi:10.1002/2004JB011707
58. O. L. Colombo, "Long range kinematic GPS" in *GPS for Geodesy, 2nd Edition*, A. Kleusberg, P. Teunissen, Eds. (Springer-Verlag, 1998).
59. O. L. Colombo, A. Sutter, A. G. Evans, Evaluation of precise, kinematic GPS point positioning. *Proceedings of ION GNSS-2004*, Long Beach, California, September, 2004.

Acknowledgments: Valuable comments from T. Nishimura improved our manuscript. We would like to thank O. L. Colombo of the NASA Goddard Space Flight Center for providing us with the kinematic GNSS software "IT" (Interferometric Translocation) (*58, 59*) and the Geospatial Information Authority of Japan (GSI) for providing us with the high-rate GNSS data for the kinematic GNSS analysis and the daily coordinates of the sites on the GSI website. The VLF catalogue was provided by Y. Asano in National Research Institute for Earth Science and Disaster Resilience (NIED). The plate models (*49, 50*) were constructed from topography and bathymetry data provided by the Geospatial Information Authority of Japan (250-m digital map), Japan Oceanographic Data Center (500-m mesh bathymetry data, J-EGG500, http://www.jodc.go.jp/jodcweb/JDOSS/infoJEGG_j.html) and the Geographic Information Network of Alaska, University of Alaska. In addition, many among the staff of the Hydrographic and Oceanographic Department, Japan Coast Guard (JHOD), including the crews of the S/Vs Takuyo, Shoyo, Meiyo, and Kaiyo, supported our observations and data processing. Some figures were produced using the GMT software; **Author contributions:** Y.Y. and T.I. designed the study and performed the statistical processing. Y.Y. carried out the grid search analysis. T.I. carried out the psuedo data analysis. Y.Y. and T.I. developed the GNSS-A seafloor geodetic observation system and wrote this manuscript; **Competing interests:** Authors declare no competing interests; and **Data and materials availability:** All data is available in the main text or the supplementary materials.

Fig. 1. Results of the SSE signal detection process off the Bungo Channel. (A) Seafloor crustal deformations detected in the SSE signal detection process. Vectors indicate seafloor crustal deformations detected in the GNSS-A data. Closed and open squares indicate the seafloor observation sites installed before and after 2011, respectively. Blue regions indicate deep SSEs detected by the onshore GEONET (*24, 25*). The yellow star indicates the epicenter of the 2016 Kumamoto earthquake. Blue dots indicate shallow VLF activities after 2013 (*11*). **(B)** Time series of seafloor crustal deformations at the sites in the green region. The maximum likelihood straight and piece-wise lines at the sites where SSE signals were not detected and were detected, respectively, are displayed. Each time series was plotted in the direction for the case of the maximum likelihood solution in the SSE signal detection process. Red lines indicate straight and piece-wise lines estimated as the maximum likelihood solutions. Grey histograms indicate Δc-AIC time series (bin range: 1 year) every 0.2 years. Each light-blue bin indicates a period judged to be an SSE signal. Bottom red histograms are shallow VLF numbers (*11*) within green region in **(A)** every month. Purple dashed lines indicate the 2011 Tohoku-oki earthquake. **(C)** Time series of onshore crustal deformations near this region. The reference frame is International Terrestrial Reference Frame 2005 (ITRF2005) (*28*). The blue region and red line indicate deformations due to deep SSE and the 2016 Kumamoto earthquake, respectively.

Fig. 2 Results of the SSE signal detection process off Tosa Bay. (A) Seafloor crustal deformations detected in the SSE signal detection process. Blue regions indicate deep SSEs detected by the onshore GEONET (*24, 25*). Blue dots indicate shallow VLF activities after 2013 (*11*). **(B)** Time series of seafloor crustal deformations at the sites in the green region. **(C)** Time series of onshore crustal deformations near this region. Other depictions are the same as in Fig. 1.

Fig. 3 Results of the SSE signal detection process off the Kii Channel. (A, A', and A'') Seafloor crustal deformations detected in the SSE signal detection process. Blue regions indicate deep SSEs detected by the onshore GEONET (*25*). Light-blue regions indicate shallow short-term SSEs (*14*). Blue dots in **A**, **A'**, and **A''** indicate shallow VLF activities between 2008 and 2009, between 2013 and 2016, and after 2017, respectively (*11*). Green focal mechanisms indicate reanalyzed VLF events (*33*). **(B)** Time series of seafloor crustal deformations at the sites in the green region. **(C)** Time series of onshore crustal deformations near this region. Other depictions are the same as in Fig. 1.

Fig. 4. Results of the SSE signal detection process around Kumano-nada. (A) Seafloor crustal deformations detected in the SSE signal detection process. Blue regions indicate deep SSEs detected by the onshore GEONET (*25, 37*). Light-blue regions indicate shallow short-term SSEs (*14*). The yellow star indicates the epicenter of the 2016 off-Mie earthquake (M_w 5.6). Blue dots indicate shallow VLF activities after 2013 (*11*). **(B)** Time series of seafloor crustal deformations at the sites in the green region. **(C)** Time series of onshore crustal deformations near this region. Other depictions are the same as in Fig. 1.

Fig. 5. Results of the SSE signal detection process around Enshu-nada. (A) Seafloor crustal deformations detected in the SSE signal detection process. Blue regions indicate deep SSEs detected by the onshore GEONET (*37*). The light-blue region indicates shallow short-term SSE activity (*14*). Blue dots indicate shallow VLF activities after 2013 (*11*). **(B)** Time series of seafloor crustal deformations at the sites in the green region. **(C)** Time series of onshore crustal deformations near this region. Other depictions are the same as in Fig. 1.

Fig. 6. Spatial relationship of seafloor sites that detected SSE signals. (A) Spatial relationship between seafloor site that detected SSE signals (red squares) and some phenomena along the Nankai Trough. Red rectangle and vector are the 2017-18 Kii Channel shallow SSE model and slip angle, respectively, estimated by the grid search when it was assumed to be due to single SSE. Pink circles indicate the shallow VLF catalog after 2006 (*11*). The light-blue polygon indicates the Kumano-nada short-term SSE activity region (*14*). The grey contour map indicates high coupling rate distribution (*17*) (rate: more than 0.5). The light-blue solid line indicates the most recent seismogenic region (*6*) (slip: more than 2 m). Blue regions indicate deep SSE regions (*24, 25, 37*) (total slip: more than 2 cm). Dashed lines indicate the depths of the plate boundary of (*52, 53*). **(B)** Shallow VLF time series compared with shallow and deep SSE timings. Black dots indicate shallow VLF activities (*11*). The red lines indicate the SSE timings detected at seafloor sites. Each yellow line indicates the longitude of the site. Blue regions indicate deep SSE periods (*24, 25, 37*). The light-blue solid line indicates the Kumano-nada short-term SSE activity region (*14*).

Science
AAAS

Supplementary Materials for

Shallow slow slip events along the Nankai Trough detected by the GNSS-A

Yusuke Yokota[1]*, Tadashi Ishikawa[2]*

Correspondence authors: Y. Yokota (yyokota@iis.u-tokyo.ac.jp) or T. Ishikawa (ishikawa@jodc.go.jp)

This PDF file includes:

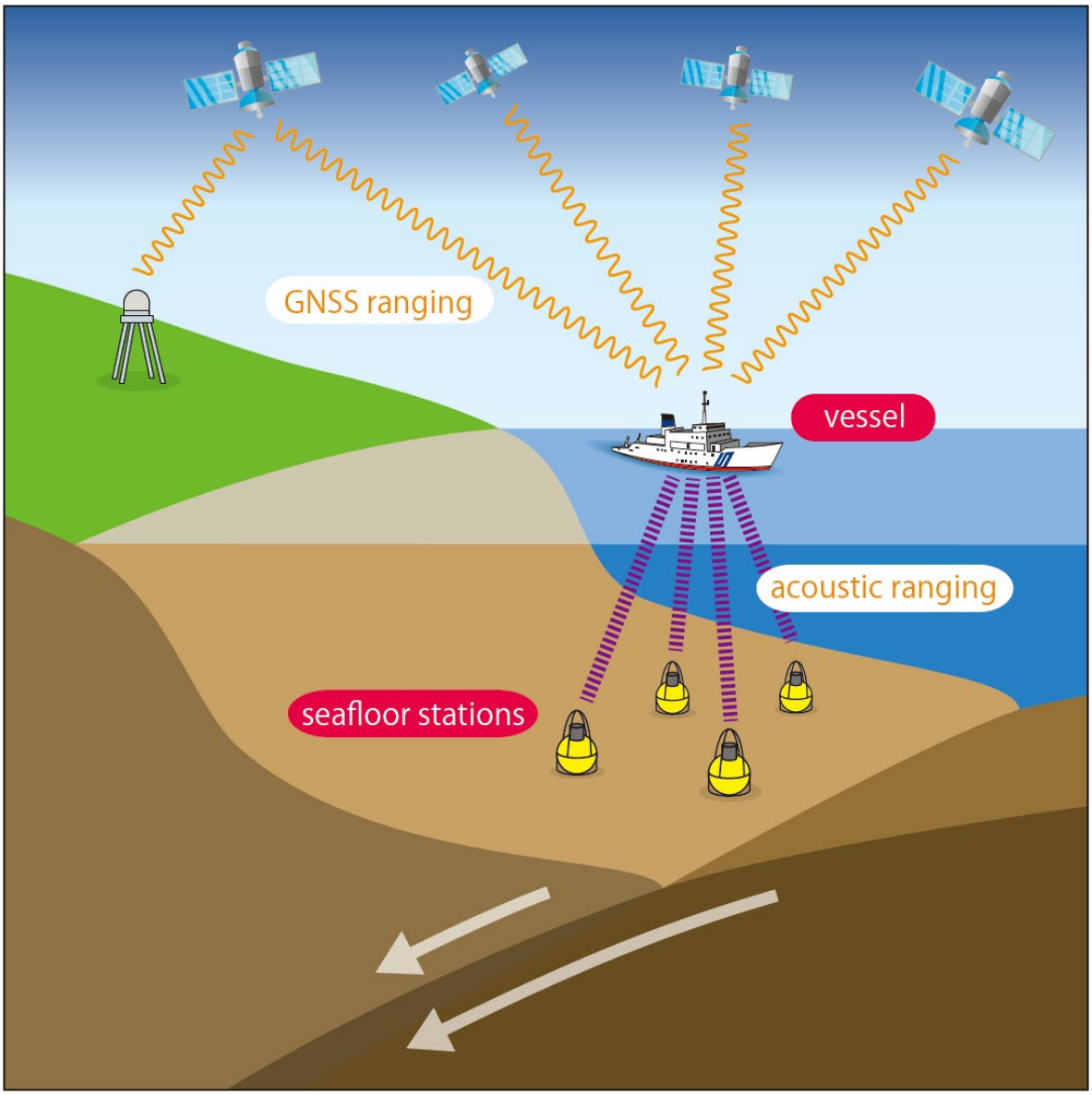

Fig. S1.
Schematic diagram of the GNSS-A seafloor geodetic observation system. This figure is modified from (*16, 20, 42-44, 50*).

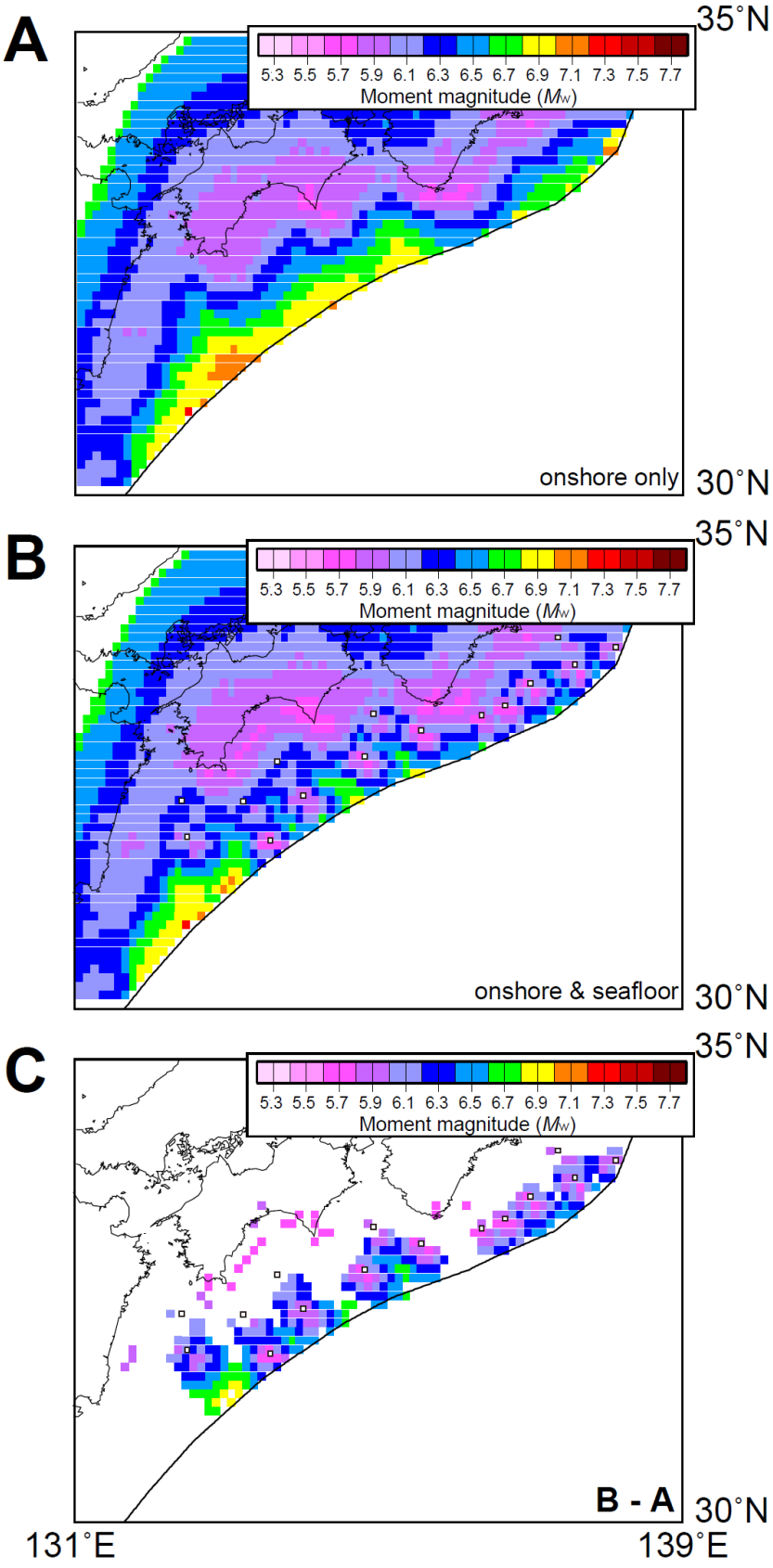
A
35˚N
5.3 5.5 5.7 5.9 6.1 6.3 6.5 6.7 6.9 7.1 7.3 7.5 7.7
Moment magnitude (M_W)
onshore only
30˚N
B
35˚N
5.3 5.5 5.7 5.9 6.1 6.3 6.5 6.7 6.9 7.1 7.3 7.5 7.7
Moment magnitude (M_W)
onshore & seafloor
30˚N
C
35˚N
5.3 5.5 5.7 5.9 6.1 6.3 6.5 6.7 6.9 7.1 7.3 7.5 7.7
Moment magnitude (M_W)
B - A
30˚N
131˚E
139˚E

Fig. S2.

Maps representing SSE detection capability constructed using (A) the onshore GNSS network only and (B) onshore and seafloor GNSS-A networks. (C) Maps representing SSEs that can be detected only by the seafloor GNSS-A network. Color points indicate the magnitude of detectable minimum events at each grid on the plate boundary.

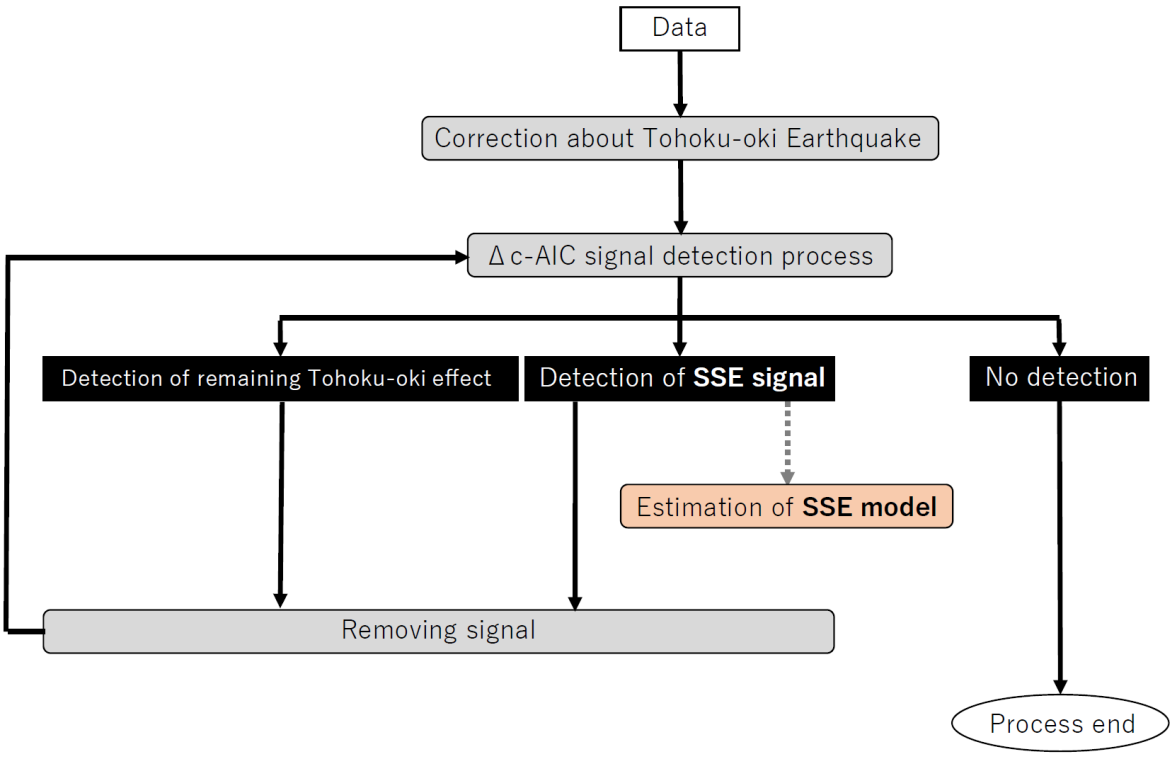

Fig. S3.
Flow of the SSE signal detection process.

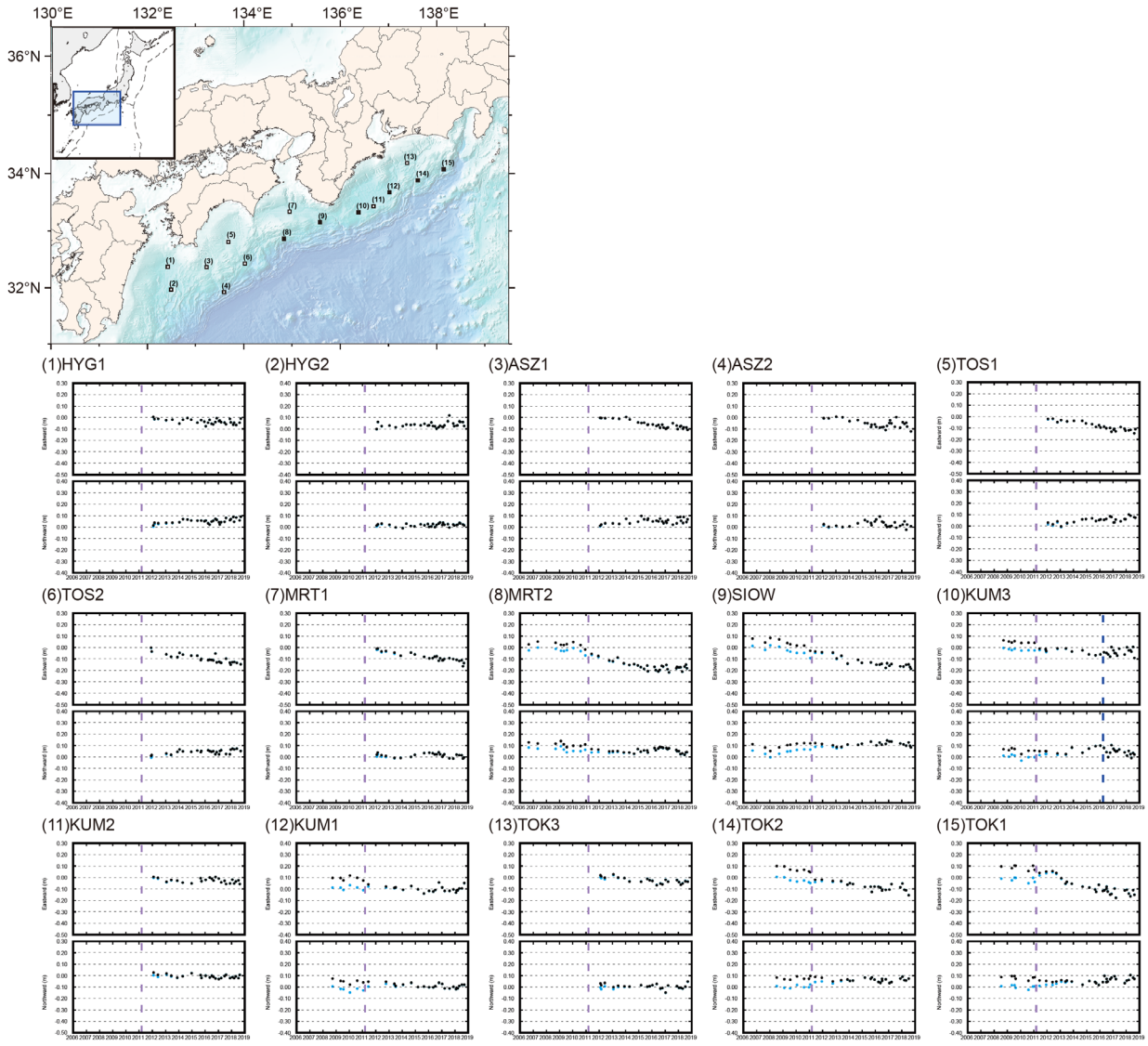

Fig. S4.

Time series of horizontal components of seafloor GNSS-A data. Black circles indicate seafloor positions after deduction of deformations due to the 2011 Tohoku-oki earthquake based on (*55-57*). Blue circles indicate raw data before deduction. The reference frame is ITRF2005 (*28*).

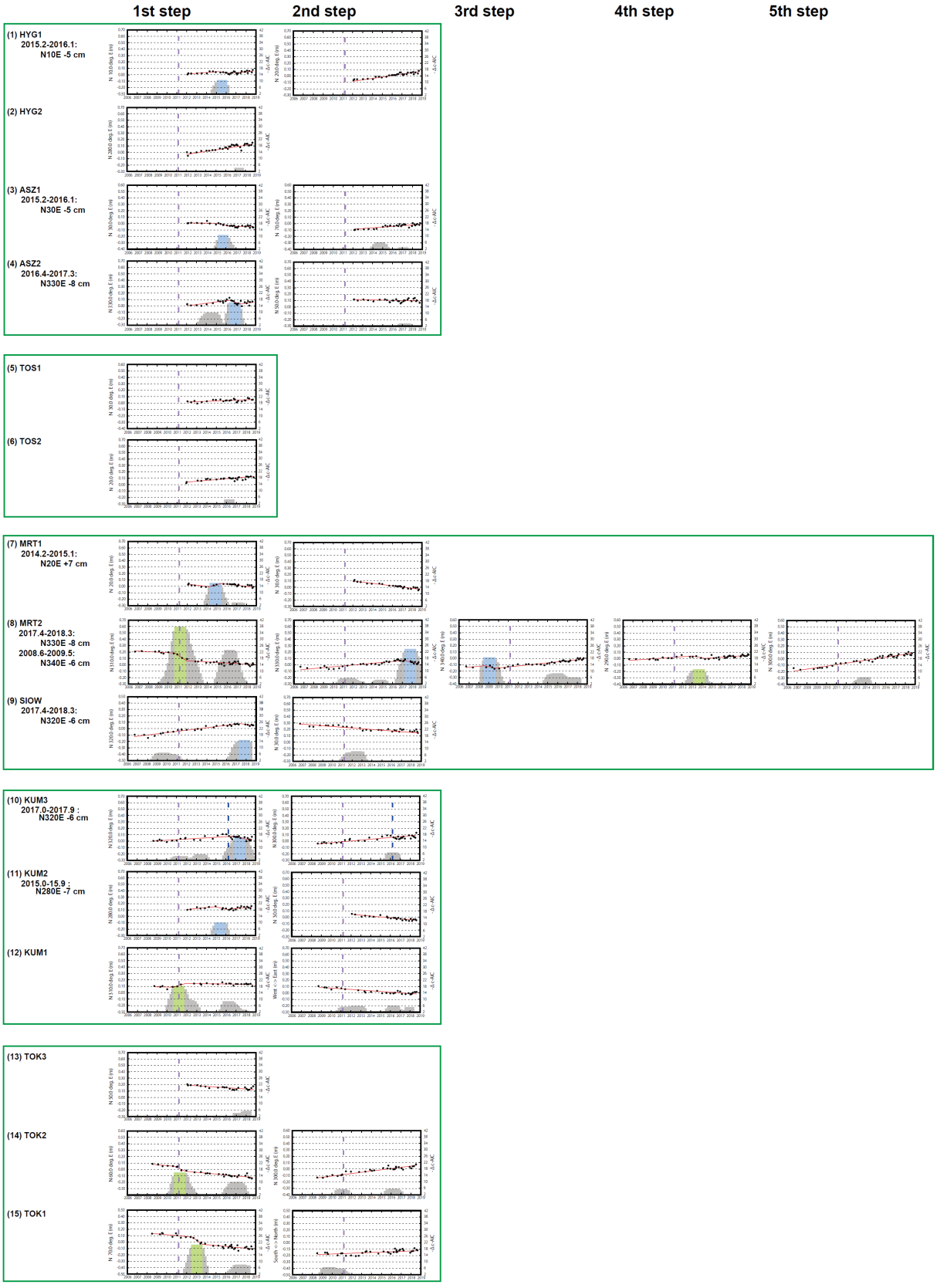
1st step
2nd step
3rd step
4th step
5th step
(1) HYG1
2015.2-2016.1:
N10E -5 cm
(2) HYG2
(3) ASZ1
2015.2-2016.1:
N30E -5 cm
(4) ASZ2
2016.4-2017.3:
N330E -8 cm
(5) TOS1
(6) TOS2
(7) MRT1
2014.2-2015.1:
N20E +7 cm
(8) MRT2
2017.4-2018.3:
N330E -8 cm
2008.6-2009.5:
N340E -6 cm
(9) SIOW
2017.4-2018.3:
N320E -6 cm
(10) KUM3
2017.0-2017.9 :
N320E -6 cm
(11) KUM2
2015.0-15.9 ;
N280E -7 cm
(12) KUM1
(13) TOK3
(14) TOK2
(15) TOK1

Fig. S5.

Results of the SSE signal detection process for all time series. Each time series was described in the direction with the maximum likelihood solution in the SSE signal detection process. The reference frame is ITRF2005 (*28*). The results for each step were obtained in order from the left. Red lines indicate straight and piece-wise lines estimated as the maximum likelihood solutions. Gray histograms are Δc-AIC time series (bin range: one year) in the process every 0.2 years. Light-blue and green bins are Δc-AIC in the cases that were judged as SSE signals and as remaining influences due to the 2011 Tohoku-oki earthquake, respectively. Purple and blue dashed lines indicate the 2011 Tohoku-oki earthquake and the 2016 M_w 5.6 earthquake in the Kumano-nada region, respectively.

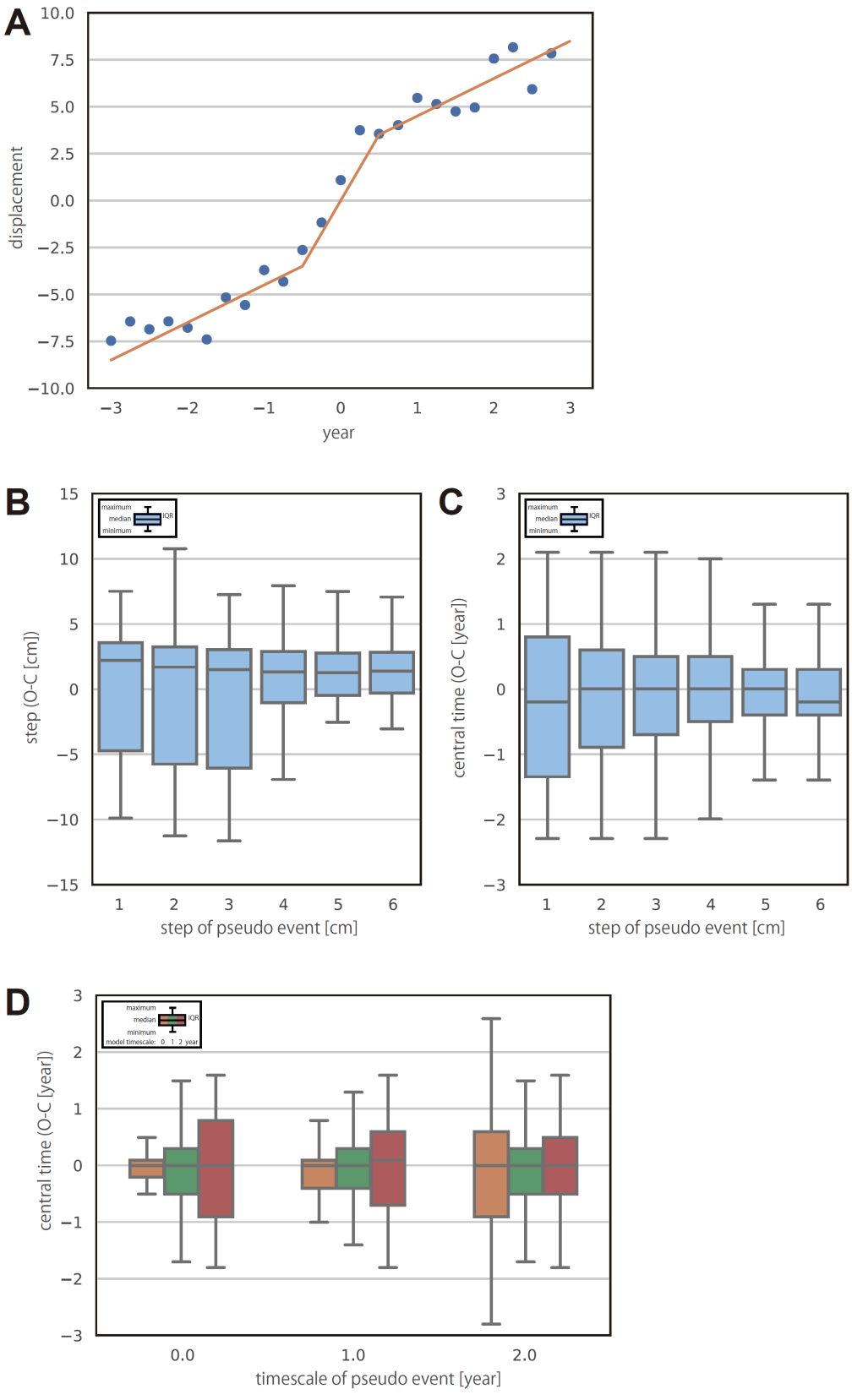
A
displacement
year
B
step (O-C [cm])
step of pseudo event [cm]
C
central time (O-C [year])
step of pseudo event [cm]
D
central time (O-C [year])
timescale of pseudo event [year]
maximum
median
minimum
IQR

Fig. S6.

Pseudo analysis test results for the SSE detection process. (A) Pseudo GNSS-A data of 6 years when deformation of 5 cm occurs in 1 year for pseudo time series data synthesized based on current observation ability (1-σ = 2.0 cm, 4 times/year). Box and whisker plots for residuals (between observation and calculation) of (B) the deformation step and (C) the central time of the event for pseudo deformation steps of 1 to 6 cm. The box and whisker ranges are the interquartile range (IQR) and a range from minimum to maximum excluding outside the range of (25 percentile – IQR * 1.5) ~ (75 percentile + IQR * 1.5), respectively. (D) Box and whisker plots for residuals (between observation and calculation) of the central time of the event. The plots show the results obtained by applying the respective models, in which the deformation timescale is 0 (orange), 1 (green), and 2 years (red), to the pseudo data when the deformation timescale is 0 (left), 1 (center), and 2 years (right).

Bungo channel

Onshore: 0 cm (< about 5 mm)

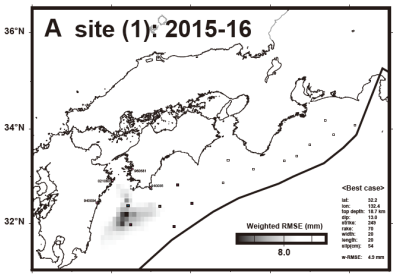

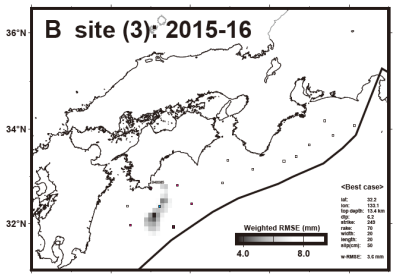

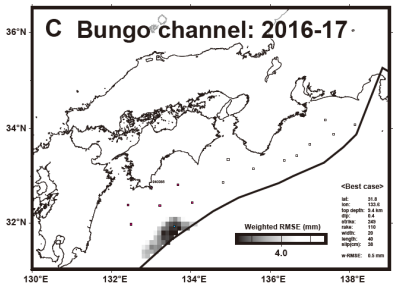

Onshore: 1 cm

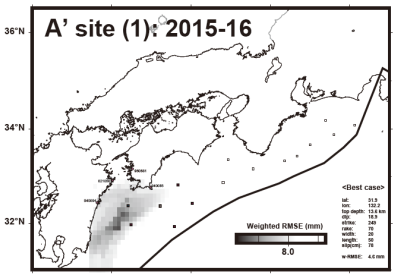

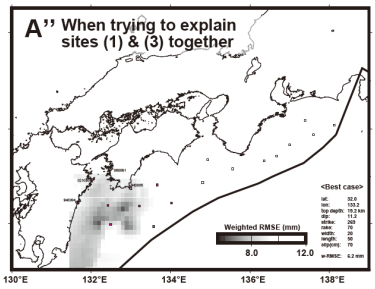

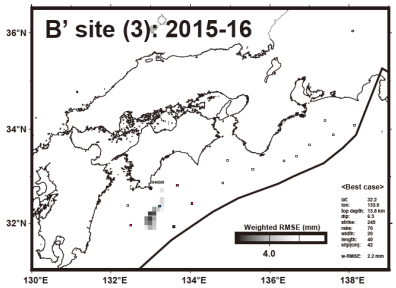

Kii channel

Onshore: 0 cm (< about 5 mm)

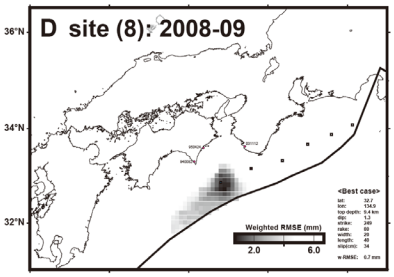

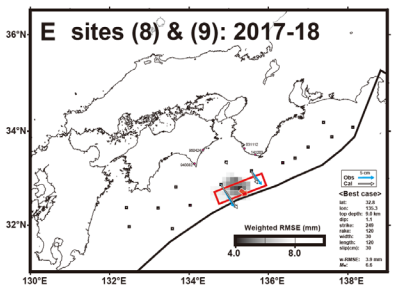

Onshore: 1 cm

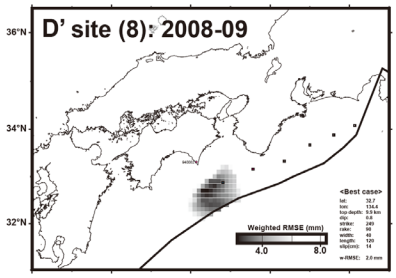

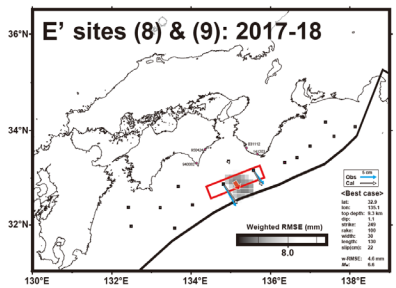

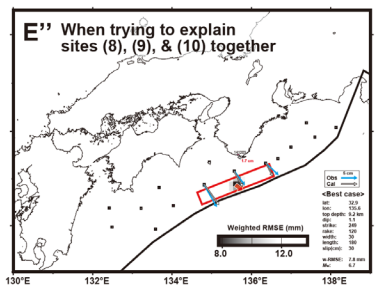

Kumano-nada

Onshore: 0 cm (< about 5 mm)

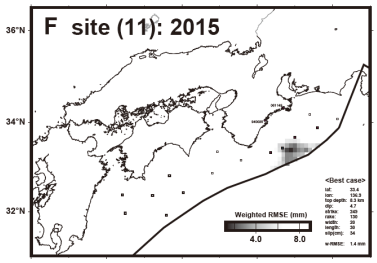

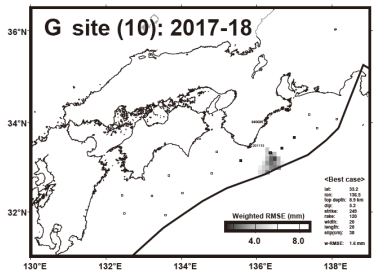

Onshore: 1 cm

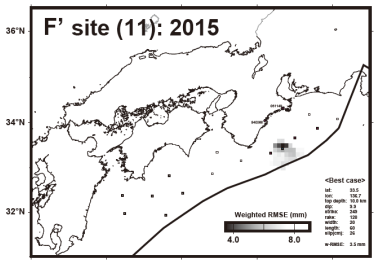

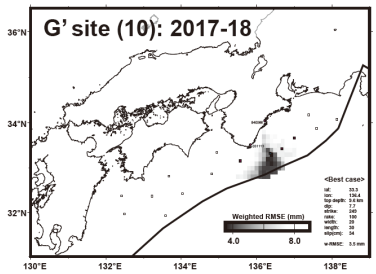

Fig. S7.

Grid search results for estimating an SSE model off the Kii Channel around 2017-18 and potential slip regions in other cases when deformations of onshore GNSS sites are 0 cm (< approximately 5 mm): (A) to (C) off the Bungo Channel around sites (1), (3), and (4) around 2015-16 and 2016-17, (D) and (E) off the Kii Channel around 2008-09 and 2017-18, and (F) and (G) around Kumano-nada around 2015 and 2017-18; and results when deformations of onshore GNSS sites are 1 cm: (A') and (B') off the Bungo Channel around sites (1) and (3) around 2015-16, (D') and (E') off the Kii Channel around 2008-09 and 2017-18, and (F') and (G') around Kumano-nada around 2015 and 2017-18. (A'') Residual distribution when trying to estimate sites (1) and (3) collectively. (D'') Residual distribution when trying to estimate sites (8), (9), and (10) collectively. Red rectangles and vectors in (D), (D'), and (D'') indicate the final obtained rectangular fault models and dip angles, respectively. Blue and white vectors in (D), (D'), and (D'') are observed and calculated movements for the sites, respectively. Grey regions indicate distributions of fault model centers with weighted RMSEs calculated in the range between the minimum and 4 mm greater than the minimum. Fault parameters of the best cases are listed at bottom right. Pink and light-blue squares and light-blue circles are the seafloor sites moved due to SSEs, unmoved sites, and onshore GEONET sites used in the grid search, respectively. GEONET site codes are described beside the sites. Open squares are the seafloor sites that were not used in the grid search.

Data file S1. (Separate file)

Time series of seafloor positions. The reference frame is ITRF2005 (*28*). The first column shows the observation epoch. The eastward and northward components (second and third columns) indicate the data corrected for the coseismic and postseismic effects due to the Tohoku-oki earthquake. The $East_{raw}$ and $North_{raw}$ components (fourth and fifth columns) are raw data before March 2014.

(1) HYG1

Epoch (year)	Eastward (m)	Northward (m)	$East_{raw}$ (m)	$North_{raw}$ (m)
2012.077	0	0	0	0
2012.162	-0.02	0.022	-0.02	0.023
2012.447	-0.018	0.019	-0.017	0.022
2013.044	-0.03	0.022	-0.029	0.028
2013.518	-0.024	0.022	-0.023	0.031
2014.047	-0.059	0.026	-0.057	0.038
2014.318	-0.025	0.054		
2014.66	-0.011	0.05		
2014.942	-0.025	0.041		
2015.411	-0.051	0.04		
2015.696	-0.029	0.041		
2015.94	-0.042	0.035		
2016.044	-0.083	0.04		
2016.219	-0.052	0.018		
2016.334	-0.026	0.005		
2016.485	-0.061	0.032		
2016.608	-0.066	0.039		
2016.775	-0.046	0.057		
2016.877	-0.013	0.046		
2017.047	-0.037	0.026		
2017.104	-0.033	0.006		
2017.208	-0.047	0.027		
2017.466	-0.051	0.03		
2017.575	-0.065	0.064		
2017.874	-0.019	0.044		
2017.94	-0.049	0.054		
2018.129	-0.069	0.073		
2018.192	-0.051	0.031		
2018.351	-0.072	0.068		
2018.605	-0.052	0.042		
2018.696	-0.017	0.074		

(2) HYG2

Epoch (year)	Eastward (m)	Northward (m)	$East_{raw}$ (m)	$North_{raw}$ (m)
2012.074	0	0	0	0

2012.17	0.062	0.011	0.062	0.011
2012.452	0.025	0.017	0.025	0.019
2013.047	0.03	0.006	0.03	0.011
2013.518	0.016	-0.017	0.017	-0.01
2014.049	0.025	-0.025	0.026	-0.016
2014.321	0.04	0.015		
2014.658	0.036	-0.005		
2014.94	0.041	-0.008		
2015.408	0.032	0.01		
2015.699	0.046	0.001		
2015.948	0.029	0.012		
2016.044	0.033	-0.013		
2016.216	0.058	-0.009		
2016.337	0.026	0.013		
2016.488	0.024	-0.015		
2016.611	0.003	0.004		
2016.775	0.016	0.016		
2016.877	0.028	0.026		
2017.047	0.02	0.004		
2017.107	0.016	0.023		
2017.208	0.032	0.006		
2017.466	0.068	0.011		
2017.575	0.119	-0.019		
2017.874	0.049	0.008		
2017.942	0.025	0		
2018.132	0.029	0.003		
2018.195	0.031	0.006		
2018.345	0.067	0.021		
2018.4	0.063	0.019		
2018.605	0.061	0.008		
2018.699	0.027	0.001		

(3) ASZ1

Epoch (year)	Eastward (m)	Northward (m)	$East_{raw}$ (m)	$North_{raw}$ (m)
2012.077	0	0	0	0
2012.159	-0.002	0.01	-0.002	0.011
2012.455	-0.003	0.021	-0.003	0.025
2013.036	-0.004	0.02	-0.002	0.027

2013.512	-0.01	0.015	-0.008	0.025
2014.044	0.008	0.06	0.011	0.072
2014.315	-0.014	0.02		
2014.945	-0.041	0.035		
2015.195	-0.045	0.085		
2015.405	-0.043	0.056		
2015.663	-0.061	0.05		
2015.701	-0.058	0.062		
2016.058	-0.058	0.037		
2016.334	-0.071	0.043		
2016.49	-0.063	0.037		
2016.614	-0.085	0.062		
2016.773	-0.06	0.038		
2016.877	-0.085	0.022		
2017.047	-0.095	0.038		
2017.107	-0.092	0.025		
2017.208	-0.084	0.049		
2017.575	-0.047	0.008		
2017.871	-0.069	0.021		
2017.942	-0.098	0.073		
2018.129	-0.077	0.075		
2018.195	-0.071	0.042		
2018.351	-0.095	0.023		
2018.397	-0.083	0.076		
2018.608	-0.084	0.032		
2018.69	-0.106	0.056		

(4) ASZ2

Epoch (year)	Eastward (m)	Northward (m)	$East_{raw}$ (m)	$North_{raw}$ (m)
2012.082	0	0	0	0
2012.088	-0.003	0.003	-0.002	0.003
2012.463	-0.002	-0.021	-0.001	-0.019
2013.033	0.012	-0.01	0.013	-0.005
2013.51	0.008	-0.022	0.009	-0.015
2014.041	-0.027	-0.017	-0.025	-0.007
2014.666	-0.018	0.011		
2015.197	-0.043	0.038		
2015.403	-0.045	0.026		

2015.666	-0.079	0.012
2015.704	-0.058	-0.006
2015.951	-0.055	0.026
2016.06	-0.077	0.044
2016.332	-0.083	0.07
2016.501	-0.079	0.025
2016.614	-0.078	0.018
2016.773	-0.105	-0.005
2016.874	-0.069	-0.022
2017.049	-0.044	-0.017
2017.107	-0.02	-0.02
2017.211	-0.046	-0.012
2017.466	-0.076	0.018
2017.578	0.009	-0.028
2017.871	-0.084	-0.011
2018.068	-0.036	-0.001
2018.197	-0.051	0.027
2018.332	-0.041	-0.046
2018.397	-0.075	-0.001
2018.688	-0.116	-0.015

(5) TOS1

Epoch (year)	Eastward (m)	Northward (m)	$East_{raw}$ (m)	$North_{raw}$ (m)
2012.074	0	0	0	0
2012.444	0.002	-0.014	0.003	-0.011
2012.786	-0.028	0.012	-0.026	0.018
2013.068	-0.011	-0.032	-0.008	-0.023
2013.521	-0.022	-0.003	-0.018	0.009
2014.038	-0.018	0.006	-0.013	0.021
2014.668	-0.018	0.029		
2014.951	-0.04	0.032		
2015.414	-0.046	0.038		
2015.707	-0.071	0.014		
2015.937	-0.056	0.022		
2016.055	-0.076	0.029		
2016.321	-0.068	0.024		
2016.49	-0.083	0.033		
2016.778	-0.08	0.056		

2016.879	-0.112	0.05
2017.049	-0.094	0.001
2017.104	-0.087	0.002
2017.205	-0.109	0.027
2017.581	-0.071	0.012
2017.877	-0.087	0.032
2017.945	-0.103	0.031
2018.192	-0.1	0.072
2018.329	-0.096	0.062
2018.608	-0.127	0.047
2018.69	-0.09	0.043

(6) TOS2

Epoch (year)	Eastward (m)	Northward (m)	$East_{raw}$ (m)	$North_{raw}$ (m)
2011.904	0	0	0	0
2011.951	-0.033	0.008	-0.033	0.008
2013.055	-0.058	0.022	-0.056	0.031
2013.419	-0.079	0.009	-0.076	0.021
2013.899	-0.083	0.036	-0.079	0.05
2014.06	-0.046	0.056	-0.043	0.072
2014.312	-0.061	0.04		
2014.948	-0.071	0.035		
2015.4	-0.071	0.047		
2015.668	-0.11	0.032		
2015.704	-0.098	0.043		
2016.222	-0.11	0.05		
2016.329	-0.106	0.043		
2016.479	-0.108	0.036		
2016.616	-0.113	0.041		
2016.773	-0.052	0.014		
2016.874	-0.129	0.033		
2017.049	-0.124	0.013		
2017.118	-0.128	0.043		
2017.211	-0.134	0.05		
2017.578	-0.096	0.017		
2017.868	-0.132	0.014		
2017.932	-0.149	0.055		
2018.068	-0.127	0.062		

2018.197	-0.125	0.057
2018.395	-0.134	0.063
2018.688	-0.146	0.043

(7) MRT1

Epoch (year)	Eastward (m)	Northward (m)	$East_{raw}$ (m)	$North_{raw}$ (m)
2012.09	0	0	0	0
2012.156	0.003	0.018	0.003	0.02
2012.438	-0.023	-0.005	-0.021	0
2012.775	-0.019	-0.011	-0.016	-0.003
2013.425	-0.042	-0.029	-0.036	-0.014
2013.896	-0.061	-0.03	-0.053	-0.01
2014.674	-0.034	-0.02		
2014.967	-0.05	-0.003		
2015.674	-0.071	0.013		
2016.063	-0.084	0.017		
2016.318	-0.083	0.013		
2016.477	-0.069	0.002		
2016.627	-0.066	0.003		
2016.778	-0.105	0.021		
2016.879	-0.084	0.003		
2017.052	-0.103	-0.019		
2017.101	-0.101	-0.01		
2017.197	-0.089	0.003		
2017.581	-0.083	-0.032		
2017.877	-0.09	-0.034		
2018.126	-0.097	-0.001		
2018.329	-0.107	-0.006		
2018.515	-0.102	-0.006		
2018.611	-0.153	-0.034		
2018.685	-0.126	-0.026		

(8) MRT2

Epoch (year)	Eastward (m)	Northward (m)	$East_{raw}$ (m)	$North_{raw}$ (m)
2006.668	0	0	0	0
2007.351	0.025	-0.01	0.024	-0.009
2008.71	0.014	-0.011	0.013	-0.011

2009.11	-0.003	0.012	-0.004	0.012
2009.332	-0.006	-0.017	-0.006	-0.017
2009.556	0.002	-0.042	0.001	-0.041
2010.049	0.021	-0.029	0.02	-0.029
2010.603	-0.006	-0.032	-0.007	-0.031
2010.956	-0.044	-0.019	-0.045	-0.018
2011.441	-0.084	-0.06	-0.04	-0.043
2011.951	-0.102	-0.064	-0.056	-0.039
2012.784	-0.142	-0.079	-0.093	-0.046
2013.058	-0.147	-0.078	-0.099	-0.042
2013.422	-0.115	-0.077	-0.065	-0.038
2013.893	-0.167	-0.088	-0.116	-0.046
2014.304	-0.181	-0.089		
2014.671	-0.173	-0.105		
2014.953	-0.184	-0.054		
2015.178	-0.199	-0.082		
2015.425	-0.215	-0.07		
2015.671	-0.186	-0.07		
2015.715	-0.235	-0.09		
2016.225	-0.197	-0.05		
2016.318	-0.226	-0.069		
2016.504	-0.237	-0.054		
2016.619	-0.225	-0.042		
2016.77	-0.188	-0.043		
2016.871	-0.194	-0.048		
2017.121	-0.18	-0.049		
2017.211	-0.218	-0.06		
2017.321	-0.245	-0.051		
2017.877	-0.21	-0.066		
2017.932	-0.197	-0.076		
2018.071	-0.203	-0.077		
2018.2	-0.2	-0.102		
2018.329	-0.239	-0.097		
2018.512	-0.194	-0.11		
2018.611	-0.177	-0.088		
2018.685	-0.21	-0.086		

(9) SIOW

Epoch (year)	Eastward (m)	Northward (m)	$East_{raw}$ (m)	$North_{raw}$ (m)
2006.693	0	0	0	0
2007.647	-0.034	-0.03	-0.034	-0.03
2008.038	0.006	-0.059	0.006	-0.059
2008.71	-0.006	-0.028	-0.006	-0.029
2009.323	-0.039	-0.009	-0.039	-0.009
2009.553	-0.05	-0.005	-0.05	-0.006
2010.047	-0.061	0.006	-0.061	0.005
2010.603	-0.061	0.01	-0.061	0.01
2011.063	-0.107	0.008	-0.107	0.008
2011.441	-0.112	0.01	-0.062	0.03
2011.948	-0.119	0.003	-0.065	0.032
2012.778	-0.122	-0.009	-0.065	0.03
2013.063	-0.174	-0.026	-0.116	0.017
2013.427	-0.15	-0.023	-0.091	0.023
2013.89	-0.218	-0.003	-0.157	0.048
2014.682	-0.185	-0.006		
2014.973	-0.212	0.005		
2015.655	-0.208	0.022		
2016.071	-0.228	-0.01		
2016.315	-0.227	0.014		
2016.474	-0.22	-0.005		
2016.781	-0.256	0.003		
2016.882	-0.216	0.032		
2017.058	-0.237	0.024		
2017.214	-0.222	0.023		
2017.879	-0.242	0.007		
2018.123	-0.244	-0.002		
2018.326	-0.228	-0.013		
2018.515	-0.226	0.015		
2018.614	-0.248	-0.014		
2018.682	-0.264	-0.028		

(10) KUM3

Epoch (year)	Eastward (m)	Northward (m)	$East_{raw}$ (m)	$North_{raw}$ (m)
2008.707	0	0	0	0
2009.112	-0.009	-0.007	-0.009	-0.008

2009.334	-0.018	0.011	-0.018	0.01
2009.551	-0.006	0.002	-0.006	0.002
2010.06	-0.022	-0.042	-0.022	-0.043
2010.6	-0.02	-0.012	-0.02	-0.013
2011.058	-0.021	-0.012	-0.021	-0.012
2011.438	-0.071	-0.017	-0.015	0.005
2011.899	-0.075	-0.016	-0.015	0.015
2011.945	-0.093	-0.017	-0.033	0.015
2012.795	-0.069	-0.036	-0.006	0.008
2013.43	-0.07	-0.042	-0.004	0.009
2013.888	-0.097	0.015	-0.029	0.07
2014.685	-0.087	-0.031		
2015.175	-0.122	0.005		
2015.677	-0.13	0.027		
2016.038	-0.122	0.031		
2016.312	-0.103	0.012		
2016.507	-0.11	-0.026		
2016.633	-0.123	-0.069		
2016.781	-0.141	-0.031		
2016.882	-0.058	0.035		
2017.033	-0.087	0.004		
2017.121	-0.111	-0.009		
2017.214	-0.114	-0.02		
2017.318	-0.133	-0.016		
2017.468	-0.072	-0.002		
2017.879	-0.123	-0.028		
2018.058	-0.06	-0.057		
2018.189	-0.088	-0.015		
2018.326	-0.087	-0.043		
2018.392	-0.098	-0.077		
2018.518	-0.057	-0.033		
2018.616	-0.154	-0.046		

(11) KUM2

Epoch (year)	Eastward (m)	Northward (m)	$East_{raw}$ (m)	$North_{raw}$ (m)
2012.093	0	0	0	0
2012.427	-0.009	-0.02	-0.008	-0.015
2013.074	-0.043	-0.009	-0.039	0.005

2013.433	-0.027	-0.028	-0.021	-0.01
2013.885	-0.033	-0.045	-0.026	-0.023
2014.299	-0.051	-0.032		
2014.975	-0.057	-0.007		
2015.652	-0.012	-0.024		
2015.723	-0.037	-0.047		
2016.036	-0.026	-0.028		
2016.348	-0.006	-0.044		
2016.507	-0.017	-0.028		
2016.633	-0.032	-0.039		
2016.784	0	-0.052		
2017.03	-0.015	-0.057		
2017.214	-0.048	-0.048		
2017.468	-0.035	-0.031		
2017.584	-0.062	-0.02		
2017.882	-0.057	-0.049		
2018.058	-0.024	-0.041		
2018.192	-0.058	-0.049		
2018.323	-0.04	-0.034		
2018.521	-0.03	-0.049		
2018.616	-0.062	-0.021		

(12) KUM1

Epoch (year)	Eastward (m)	Northward (m)	$East_{raw}$ (m)	$North_{raw}$ (m)
2008.729	0	0	0	0
2009.337	0	-0.02	-0.001	-0.02
2009.551	-0.02	-0.024	-0.021	-0.024
2010.041	0.021	-0.053	0.021	-0.053
2010.597	0.001	-0.018	0.001	-0.018
2011.055	-0.022	-0.034	-0.022	-0.034
2011.438	-0.056	-0.027	0.011	0
2012.773	-0.074	-0.027	0.003	0.025
2013.408	-0.086	-0.045	-0.006	0.015
2013.507	-0.081	-0.063	0	-0.002
2014.066	-0.103	-0.052	-0.019	0.016
2014.69	-0.07	-0.036		
2015.2	-0.099	-0.074		
2015.647	-0.136	-0.069		

2016.036	-0.113	-0.076
2016.351	-0.118	-0.076
2016.51	-0.104	-0.066
2016.784	-0.039	-0.036
2017.03	-0.082	-0.046
2017.216	-0.113	-0.085
2017.584	-0.113	-0.086
2017.882	-0.1	-0.072
2018.074	-0.128	-0.091
2018.121	-0.109	-0.081
2018.203	-0.108	-0.086
2018.323	-0.092	-0.064
2018.521	-0.092	-0.053
2018.701	-0.044	-0.053

(13) TOK3

Epoch (year)	Eastward (m)	Northward (m)	$East_{raw}$ (m)	$North_{raw}$ (m)
2012.096	0	0	0	0
2012.153	-0.01	-0.015	-0.01	-0.014
2012.422	-0.022	0.004	-0.019	0.012
2013.077	0.009	-0.032	0.017	-0.013
2013.436	-0.02	-0.02	-0.009	0.005
2013.91	-0.025	-0.026	-0.009	0.006
2014.293	-0.055	-0.028		
2015.17	-0.056	-0.015		
2015.644	-0.032	-0.029		
2015.825	-0.044	-0.024		
2016.033	-0.05	-0.015		
2016.353	-0.088	-0.004		
2016.636	-0.073	-0.045		
2016.786	-0.079	-0.04		
2017.03	-0.04	-0.081		
2017.216	-0.056	-0.018		
2017.885	-0.042	-0.024		
2018.044	-0.06	-0.038		
2018.181	-0.083	-0.037		
2018.321	-0.072	-0.045		
2018.521	-0.052	-0.029		

2018.704	-0.056	0.017

(14) TOK2

Epoch (year)	Eastward (m)	Northward (m)	$East_{raw}$ (m)	$North_{raw}$ (m)
2008.529	0	0	0	0
2009.104	-0.003	-0.014	-0.003	-0.014
2009.548	-0.03	-0.019	-0.031	-0.019
2010.063	-0.04	0.011	-0.04	0.011
2010.595	-0.032	-0.01	-0.032	-0.01
2010.964	-0.047	-0.01	-0.047	-0.01
2011.066	-0.053	0.014	-0.053	0.014
2011.436	-0.119	0.006	-0.045	0.037
2011.942	-0.118	-0.002	-0.036	0.043
2012.77	-0.13	-0.033	-0.044	0.026
2013.405	-0.131	-0.023	-0.041	0.045
2013.882	-0.162	-0.016	-0.069	0.057
2014.068	-0.149	-0.029	-0.055	0.047
2014.296	-0.157	-0.027		
2015.203	-0.182	0		
2015.641	-0.18	-0.01		
2015.726	-0.226	0.001		
2015.932	-0.18	-0.019		
2016.227	-0.181	-0.039		
2016.378	-0.188	-0.046		
2016.512	-0.206	-0.028		
2016.501	-0.214	-0.012		
2016.784	-0.208	-0.016		
2017.06	-0.206	-0.048		
2017.216	-0.157	-0.04		
2017.885	-0.186	-0.009		
2018.044	-0.152	0.007		
2018.192	-0.207	-0.024		
2018.321	-0.212	-0.026		
2018.523	-0.255	-0.009		

(15) TOK1

Epoch (year)	Eastward (m)	Northward (m)	$East_{raw}$ (m)	$North_{raw}$ (m)

2008.54	0	0	0	0
2009.34	-0.014	0.009	-0.014	0.009
2009.545	0.009	0.009	0.009	0.009
2009.627	0.007	-0.014	0.007	-0.014
2010.595	-0.039	-0.032	-0.04	-0.032
2010.948	0.008	-0.003	0.008	-0.004
2011.068	-0.028	-0.002	-0.028	-0.002
2011.436	-0.056	-0.029	0.027	0.005
2011.942	-0.045	-0.034	0.048	0.014
2012.419	-0.04	-0.044	0.056	0.013
2012.71	-0.056	-0.038	0.042	0.024
2013.085	-0.102	-0.027	-0.002	0.041
2013.403	-0.148	-0.038	-0.046	0.035
2013.501	-0.132	-0.03	-0.03	0.044
2013.879	-0.15	-0.038	-0.045	0.041
2014.693	-0.176	-0.067		
2015.205	-0.184	-0.034		
2015.641	-0.201	-0.043		
2015.726	-0.221	-0.052		
2015.923	-0.16	-0.069		
2016.23	-0.214	-0.044		
2016.356	-0.208	0.011		
2016.515	-0.176	-0.016		
2016.504	-0.195	-0.044		
2016.597	-0.218	-0.04		
2016.786	-0.245	-0.019		
2016.885	-0.239	-0.005		
2017.123	-0.193	0.007		
2017.219	-0.275	-0.017		
2017.888	-0.209	-0.053		
2018.041	-0.203	-0.031		
2018.195	-0.237	-0.026		
2018.318	-0.261	0.017		
2018.523	-0.207	-0.006		
2018.619	-0.247	-0.016		

Fig 1

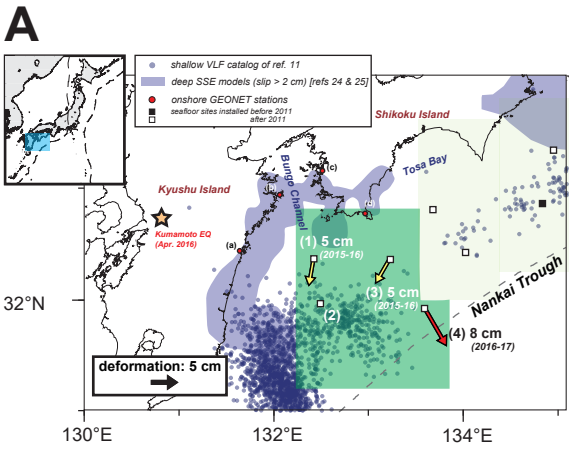
A
shallow VLF catalog of ref. 11
deep SSE models (slip > 2 cm) [refs 24 & 25]
onshore GEONET stations
seafloor sites installed before 2011
after 2011
Shikoku Island
Kyushu Island
Bungo Channel
Tosa Bay
Nankai Trough
Kumamoto EQ
(Apr. 2016)
(1) 5 cm
(2015-16)
(2)
(3) 5 cm
(2015-16)
(4) 8 cm
(2016-17)
deformation: 5 cm
32°N
130°E
132°E
134°E

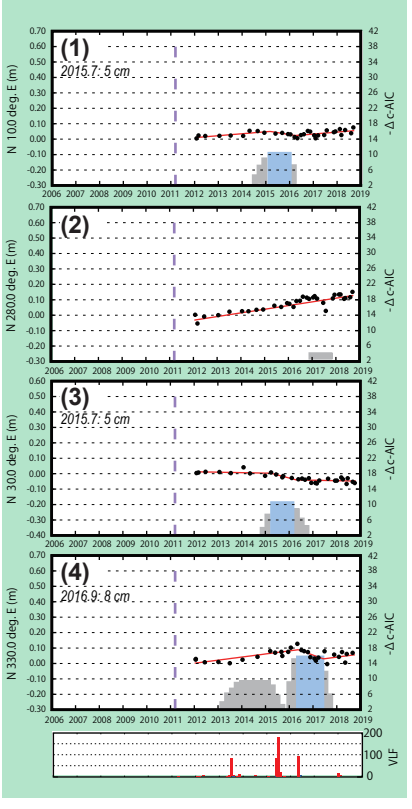
B
(1)
2015.7: 5 cm
(2)
(3)
2015.7: 5 cm
(4)
2016.9: 8 cm
N 10.0 deg.E (m)
N 280.0 deg.E (m)
N 30.0 deg.E (m)
N 330.0 deg.E (m)
-Δ c-AIC
VLF

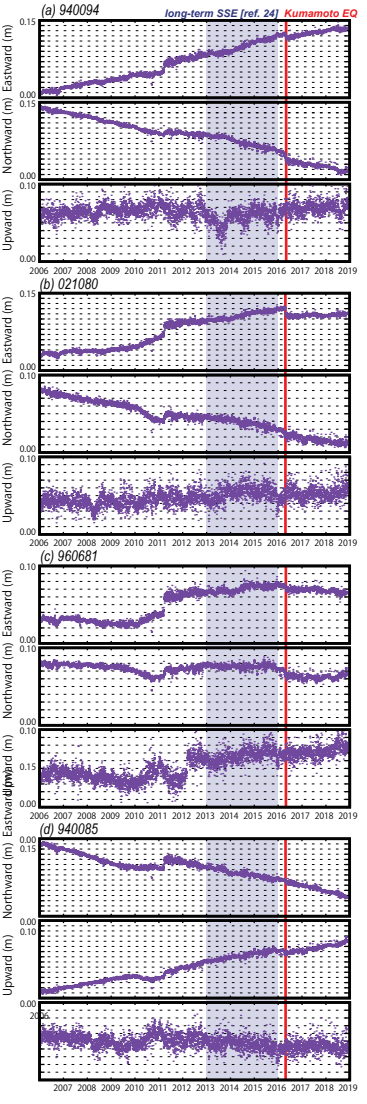
C
(a) 940094
long-term SSE [ref. 24]
Kumamoto EQ
(b) 021080
(c) 960681
(d) 940085
Eastward (m)
Northward (m)
Upward (m)

Fig 2

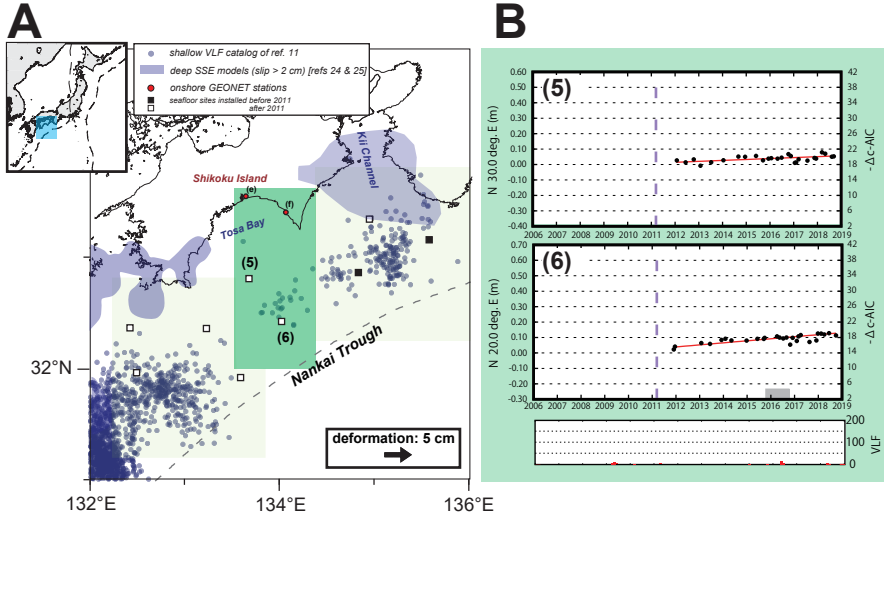
A
shallow VLF catalog of ref. 11
deep SSE models (slip > 2 cm) [refs 24 & 25]
onshore GEONET stations
seafloor sites installed before 2011
after 2011
Shikoku Island
Kii Channel
Tosa Bay
(e)
(f)
(5)
(6)
Nankai Trough
32°N
132°E
134°E
136°E
deformation: 5 cm
B
(5)
(6)
N 30.0 deg. E (m)
N 20.0 deg. E (m)
- Δc-AIC
VLF
2006 2007 2008 2009 2010 2011 2012 2013 2014 2015 2016 2017 2018 2019
C
(e) 940083
(f) 950444
Eastward (m)
Northward (m)
Upward (m)
2006 2007 2008 2009 2010 2011 2012 2013 2014 2015 2016 2017 2018 2019

Fig 3

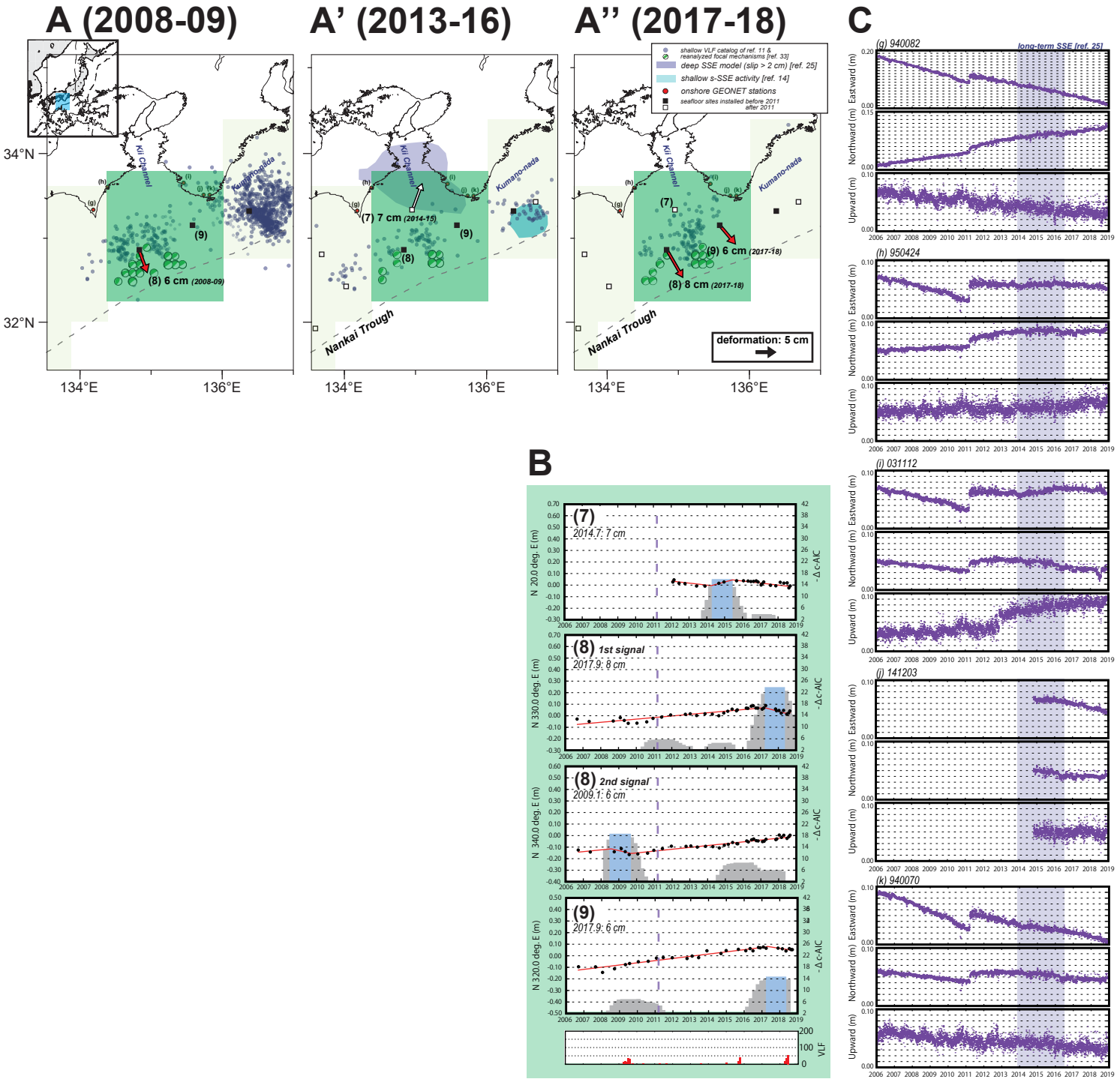
A (2008-09)
A' (2013-16)
A'' (2017-18)
C
B
shallow VLF catalog of ref. 11 & reanalyzed focal mechanisms [ref. 33]
deep SSE model (slip > 2 cm) [ref. 25]
shallow s-SSE activity [ref. 14]
onshore GEONET stations
seafloor sites installed before 2011
after 2011
Kii Channel
Kumano-nada
Nankai Trough
34°N
32°N
134°E
136°E
(7) 7 cm (2014-15)
(8) 6 cm (2008-09)
(9) 6 cm (2017-18)
(8) 8 cm (2017-18)
deformation: 5 cm
long-term SSE [ref. 25]
(g) 940082
(h) 950424
(i) 031112
(j) 141203
(k) 940070
Eastward (m)
Northward (m)
Upward (m)
(7) 2014.7: 7 cm
(8) 1st signal 2017.9: 8 cm
(8) 2nd signal 2009.1: 6 cm
(9) 2017.9: 6 cm
N 20.0 deg. E (m)
N 330.0 deg. E (m)
N 340.0 deg. E (m)
N 320.0 deg. E (m)
- Δ c-AIC
VLF

Fig 4

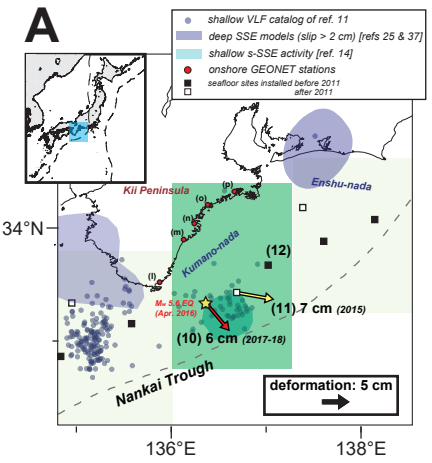
A
shallow VLF catalog of ref. 11
deep SSE models (slip > 2 cm) [refs 25 & 37]
shallow s-SSE activity [ref. 14]
onshore GEONET stations
seafloor sites installed before 2011
after 2011
Kii Peninsula
Enshu-nada
Kumano-nada
Nankai Trough
(12)
(11) 7 cm (2015)
(10) 6 cm (2017-18)
Mw 5.6EQ (Apr. 2016)
deformation: 5 cm
34°N
136°E
138°E

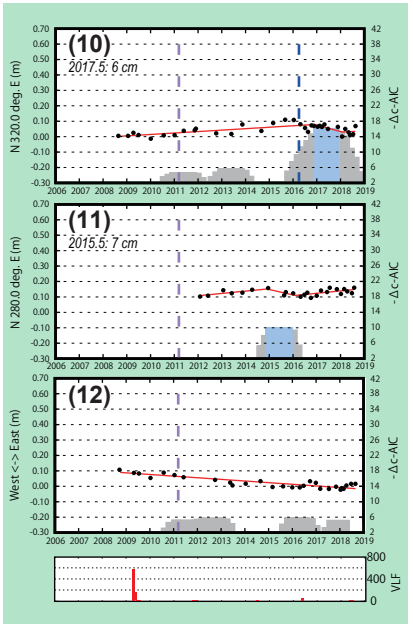
B
(10)
2017.5: 6 cm
(11)
2015.5: 7 cm
(12)
N 320.0 deg. E (m)
N 280.0 deg. E (m)
West <-> East (m)
- Δc-AIC
VLF

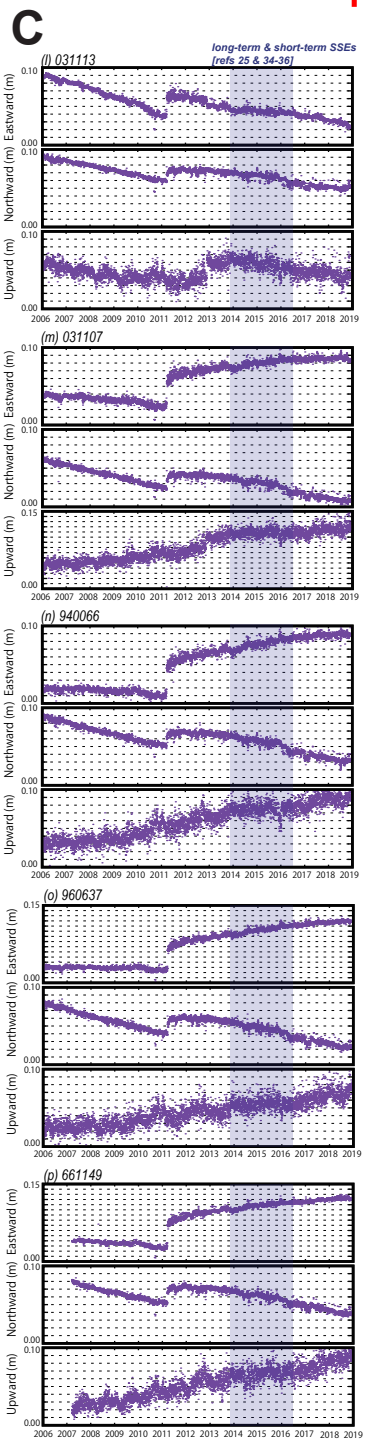
C
long-term & short-term SSEs
[refs 25 & 34-36]
(l) 031113
(m) 031107
(n) 940066
(o) 960637
(p) 661149
Eastward (m)
Northward (m)
Upward (m)

Fig 5

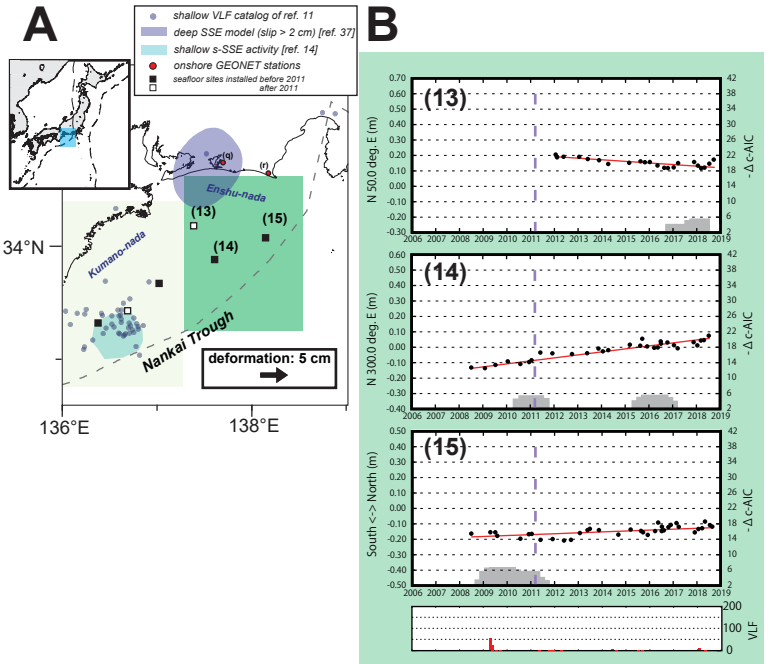
A
shallow VLF catalog of ref. 11
deep SSE model (slip > 2 cm) [ref. 37]
shallow s-SSE activity [ref. 14]
onshore GEONET stations
seafloor sites installed before 2011
after 2011
(q)
(r)
Enshu-nada
(13)
(15)
(14)
Kumano-nada
Nankai Trough
deformation: 5 cm
34°N
136°E
138°E
B
(13)
(14)
(15)
N 50.0 deg. E (m)
N 300.0 deg. E (m)
South <-> North (m)
-Δ c-AIC
VLF
C
(q) 041136
long-term SSE [ref. 37]
(r) 960625
Eastward (m)
Northward (m)
Upward (m)

Fig 6

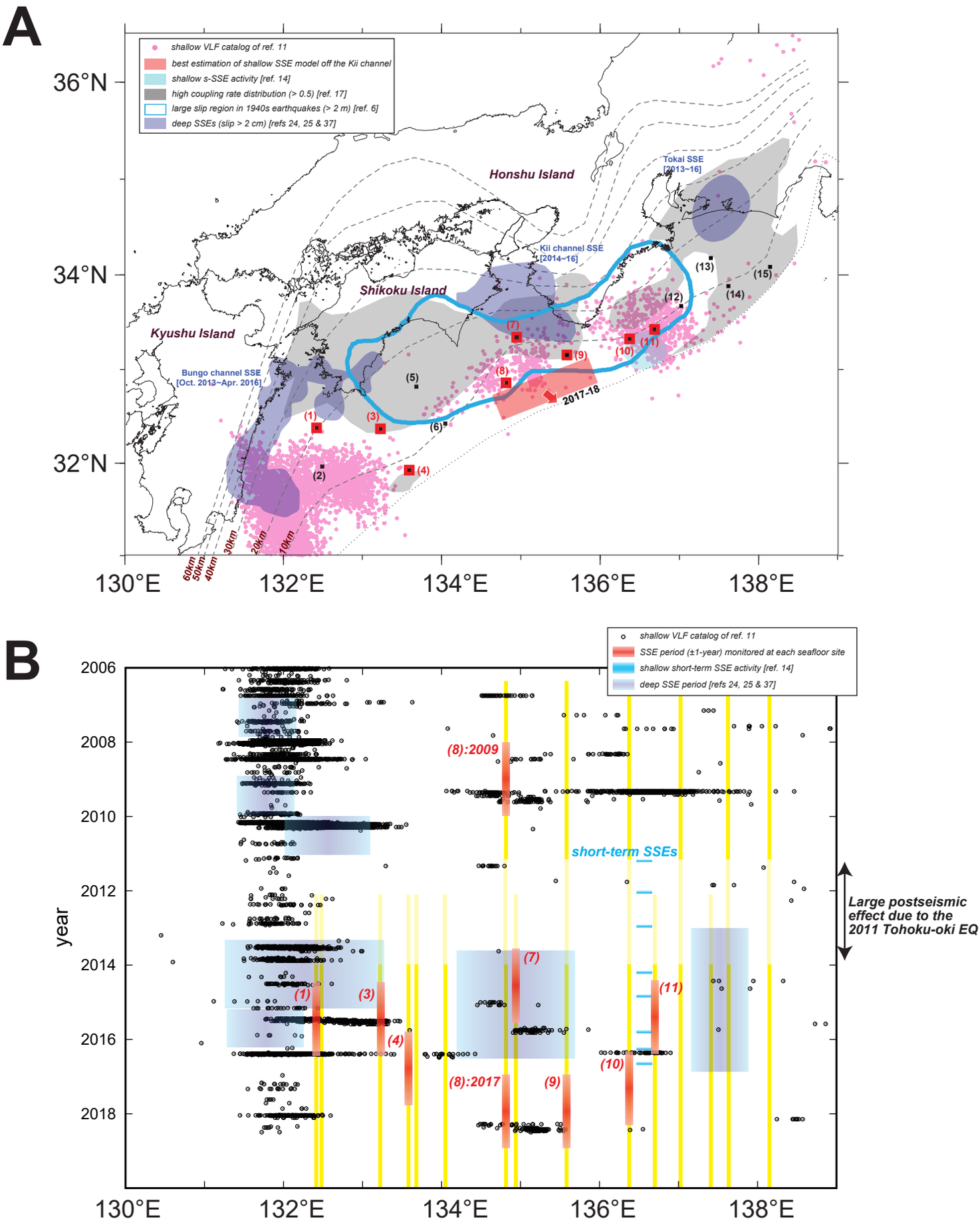
A
shallow VLF catalog of ref. 11
best estimation of shallow SSE model off the Kii channel
shallow s-SSE activity [ref. 14]
high coupling rate distribution (> 0.5) [ref. 17]
large slip region in 1940s earthquakes (> 2 m) [ref. 6]
deep SSEs (slip > 2 cm) [refs 24, 25 & 37]
Honshu Island
Shikoku Island
Kyushu Island
Tokai SSE [2013~16]
Kii channel SSE [2014~16]
Bungo channel SSE [Oct. 2013~Apr. 2016]
2017-18
(1)
(2)
(3)
(4)
(5)
(6)
(7)
(8)
(9)
(10)
(11)
(12)
(13)
(14)
(15)
60km
50km
40km
30km
20km
10km
36°N
34°N
32°N
130°E
132°E
134°E
136°E
138°E
B
shallow VLF catalog of ref. 11
SSE period (±1-year) monitored at each seafloor site
shallow short-term SSE activity [ref. 14]
deep SSE period [refs 24, 25 & 37]
year
2006
2008
2010
2012
2014
2016
2018
(8):2009
short-term SSEs
Large postseismic effect due to the 2011 Tohoku-oki EQ
(1)
(3)
(4)
(7)
(11)
(10)
(8):2017
(9)
130°E
132°E
134°E
136°E
138°E

Fig S1

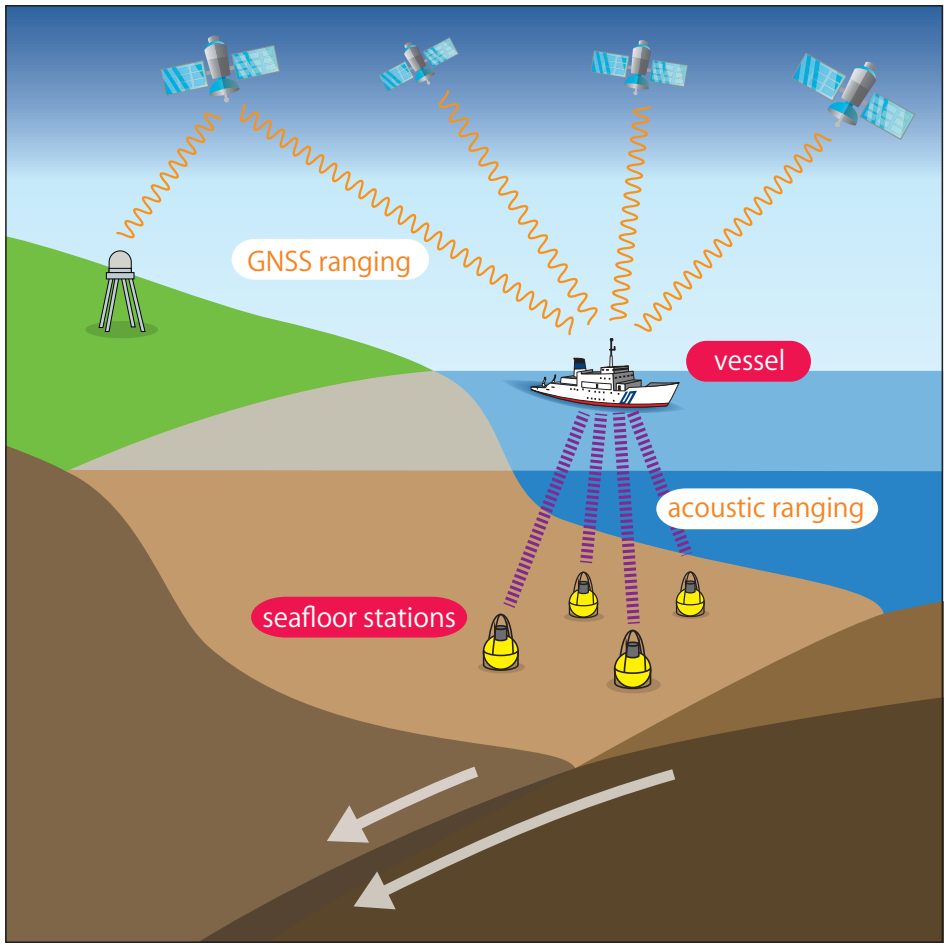

Fig S2

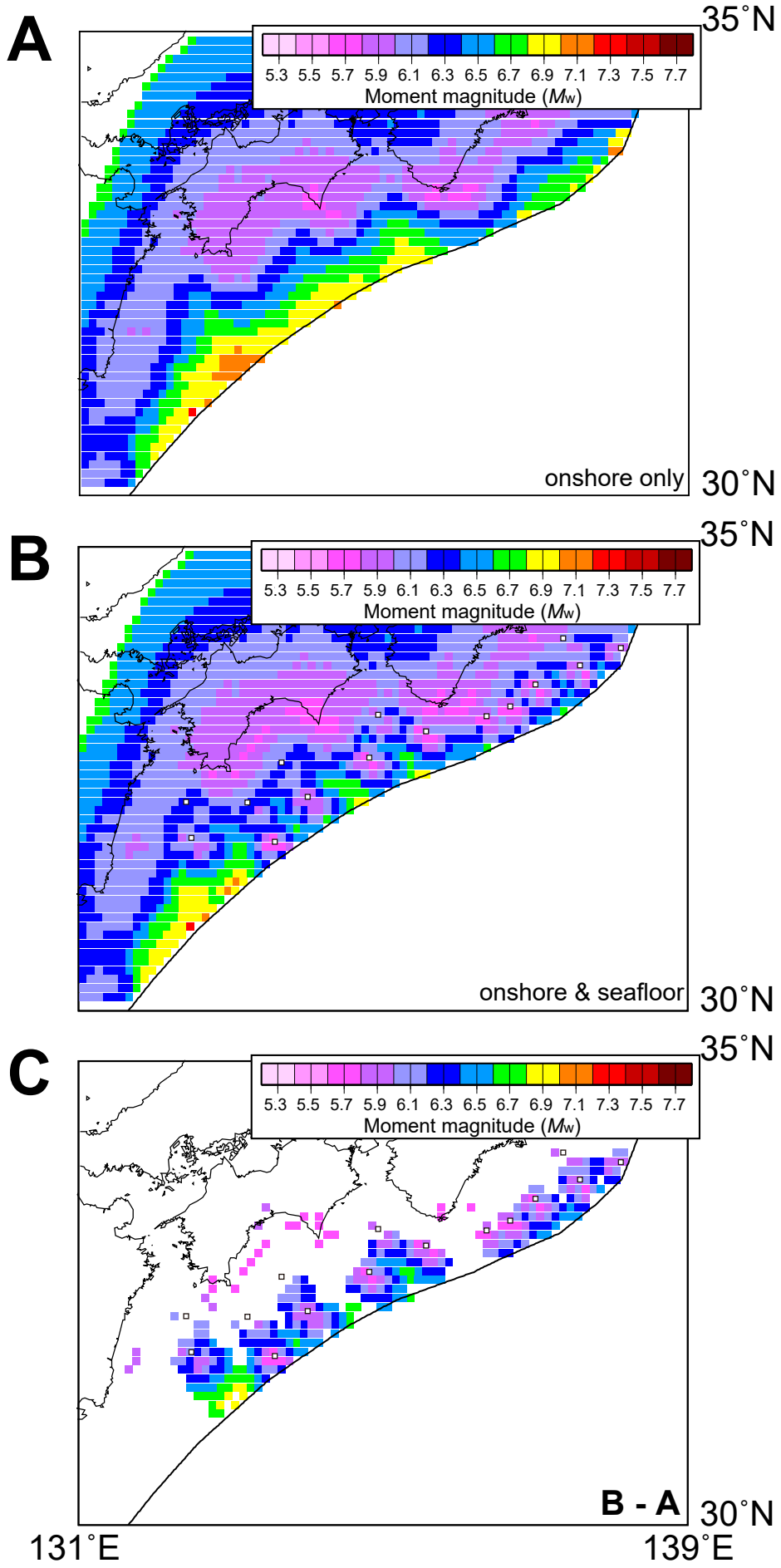
A
35˚N
5.3 5.5 5.7 5.9 6.1 6.3 6.5 6.7 6.9 7.1 7.3 7.5 7.7
Moment magnitude (Mw)
onshore only
30˚N
B
35˚N
5.3 5.5 5.7 5.9 6.1 6.3 6.5 6.7 6.9 7.1 7.3 7.5 7.7
Moment magnitude (Mw)
onshore & seafloor
30˚N
C
35˚N
5.3 5.5 5.7 5.9 6.1 6.3 6.5 6.7 6.9 7.1 7.3 7.5 7.7
Moment magnitude (Mw)
B - A
30˚N
131˚E
139˚E

Fig S3

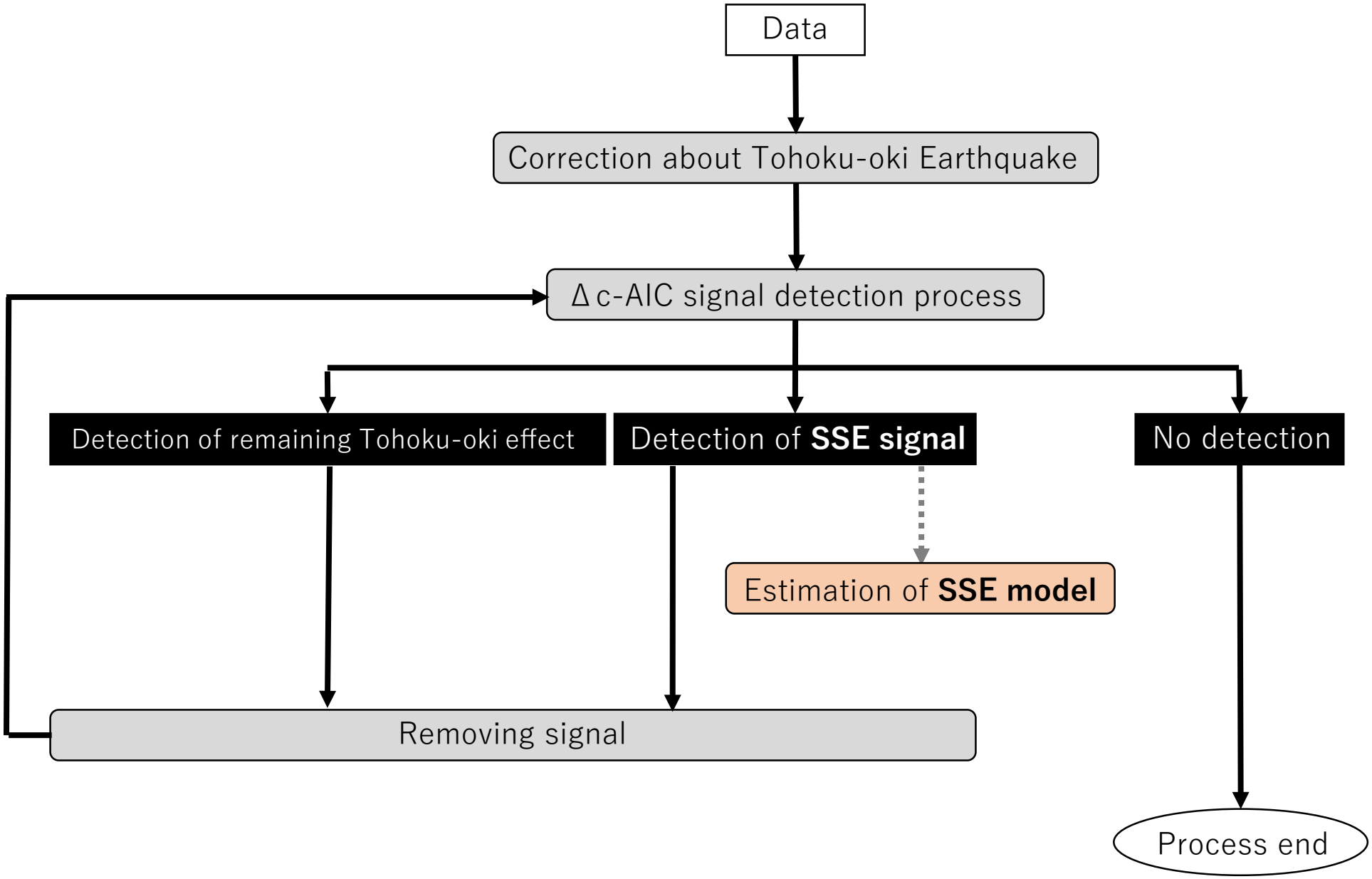
Data
Correction about Tohoku-oki Earthquake
Δc-AIC signal detection process
Detection of remaining Tohoku-oki effect
Detection of **SSE signal**
No detection
Estimation of **SSE model**
Removing signal
Process end

Fig S4

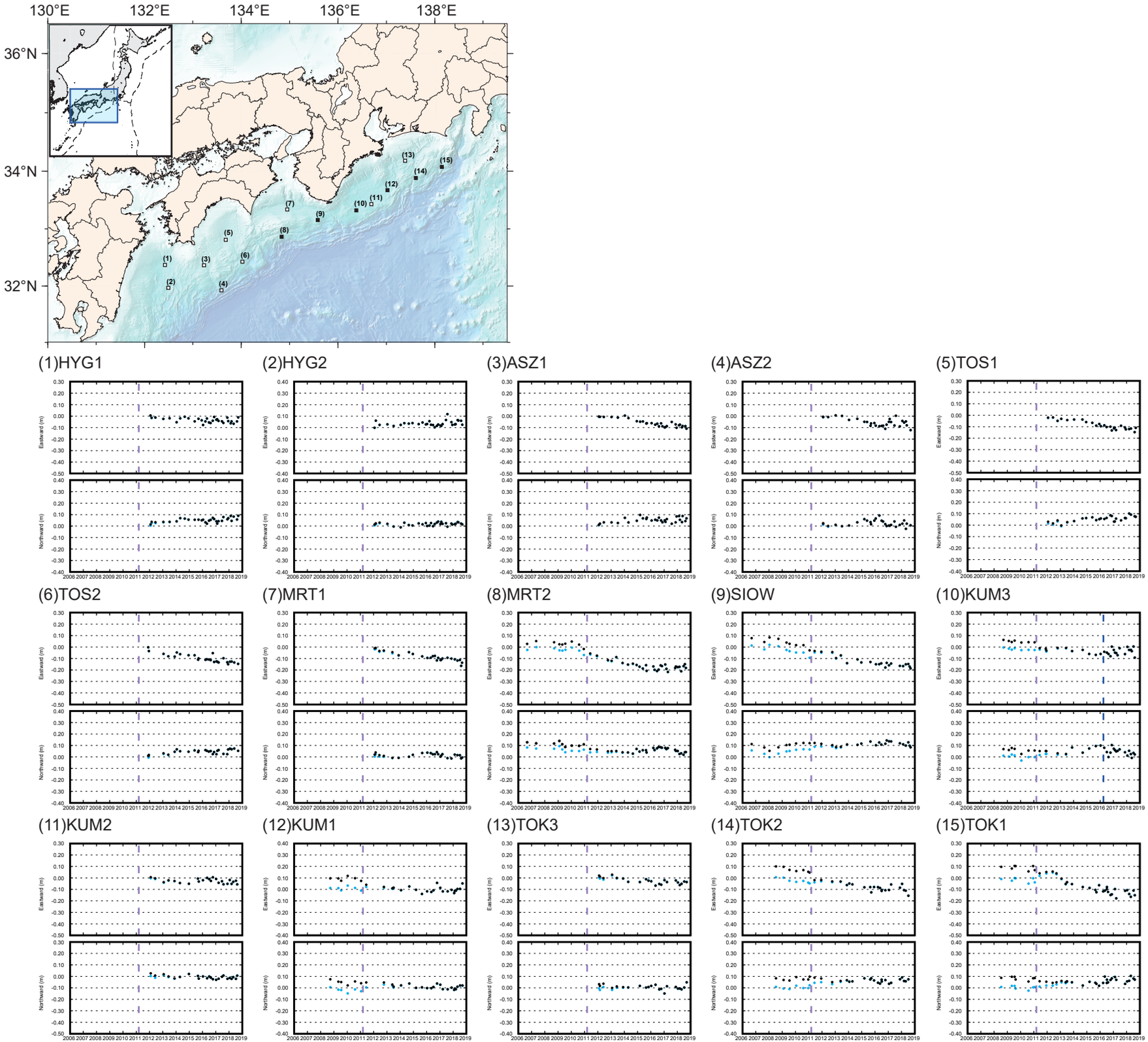
130°E
132°E
134°E
136°E
138°E
36°N
34°N
32°N
(1)
(2)
(3)
(4)
(5)
(6)
(7)
(8)
(9)
(10)
(11)
(12)
(13)
(14)
(15)
(1)HYG1
(2)HYG2
(3)ASZ1
(4)ASZ2
(5)TOS1
(6)TOS2
(7)MRT1
(8)MRT2
(9)SIOW
(10)KUM3
(11)KUM2
(12)KUM1
(13)TOK3
(14)TOK2
(15)TOK1
Eastward (m)
Northward (m)
2006 2007 2008 2009 2010 2011 2012 2013 2014 2015 2016 2017 2018 2019

Fig S5

	1st step	2nd step	3rd step	4th step	5th step
(1) HYG1 2015.2-2016.1: N10E -5 cm	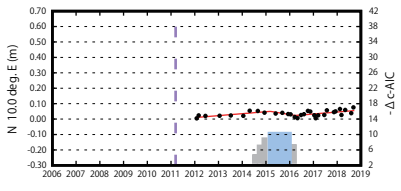	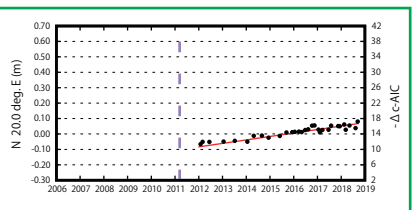			
(2) HYG2	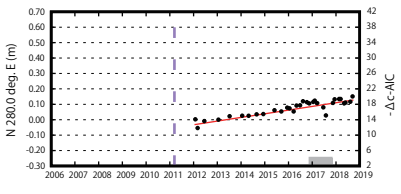				
(3) ASZ1 2015.2-2016.1: N30E -5 cm	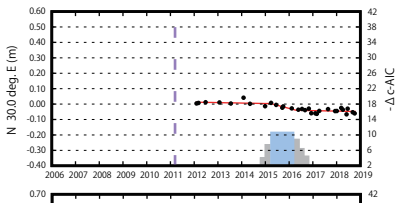	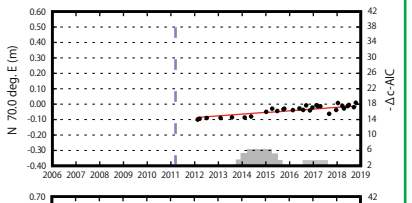			
(4) ASZ2 2016.4-2017.3: N330E -8 cm	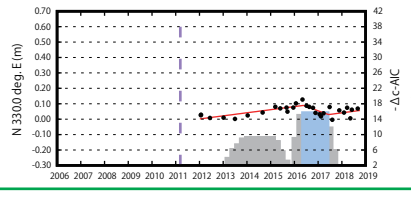	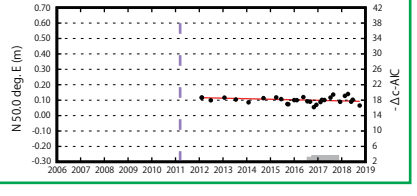			
(5) TOS1	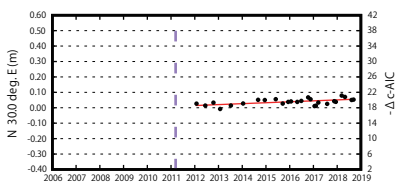				
(6) TOS2	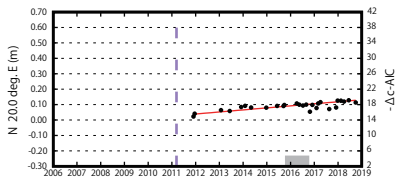				
(7) MRT1 2014.2-2015.1: N20E +7 cm	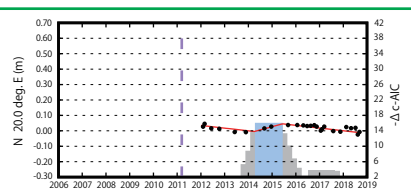	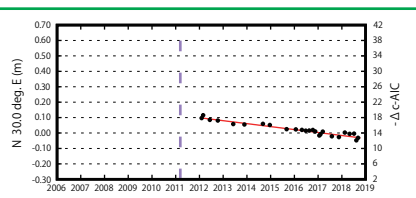			
(8) MRT2 2017.4-2018.3: N330E -8 cm 2008.6-2009.5: N340E -6 cm	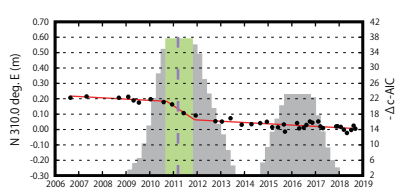	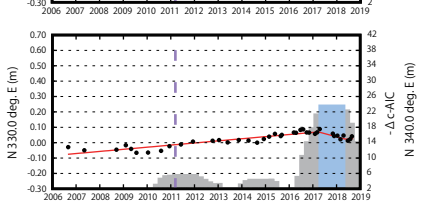	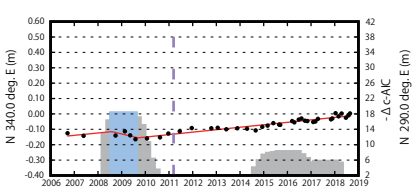	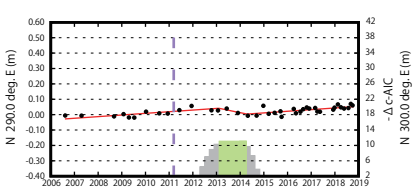	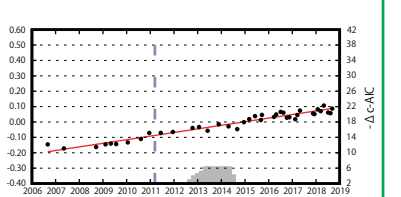
(9) SIOW 2017.4-2018.3: N320E -6 cm	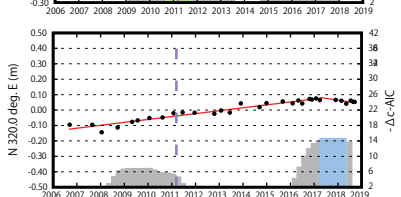	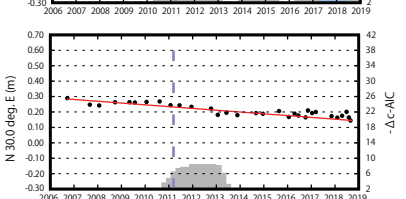			
(10) KUM3 2017.0-2017.9 : N320E -6 cm	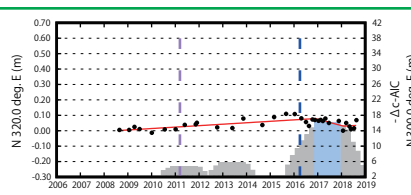	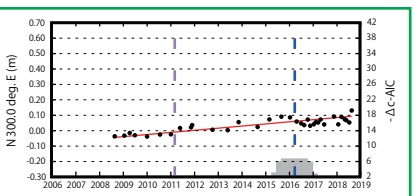			
(11) KUM2 2015.0-15.9 : N280E -7 cm					
(12) KUM1	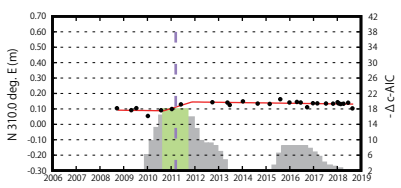	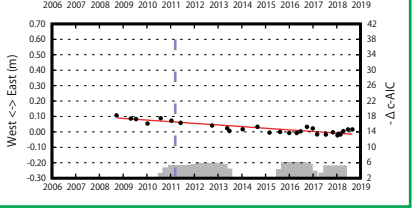			
(13) TOK3	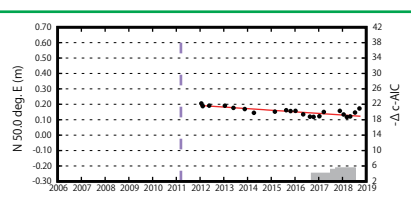				
(14) TOK2	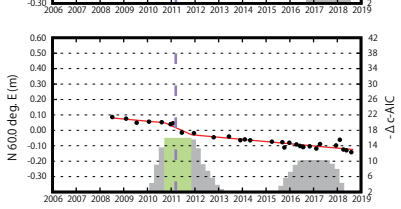	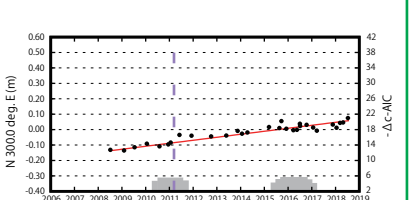			
(15) TOK1	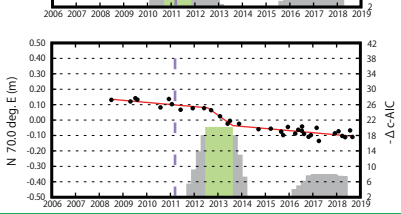	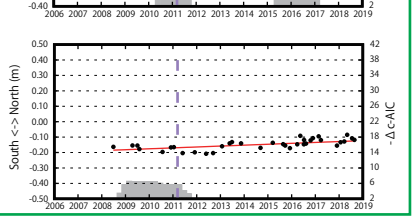			

Fig S6

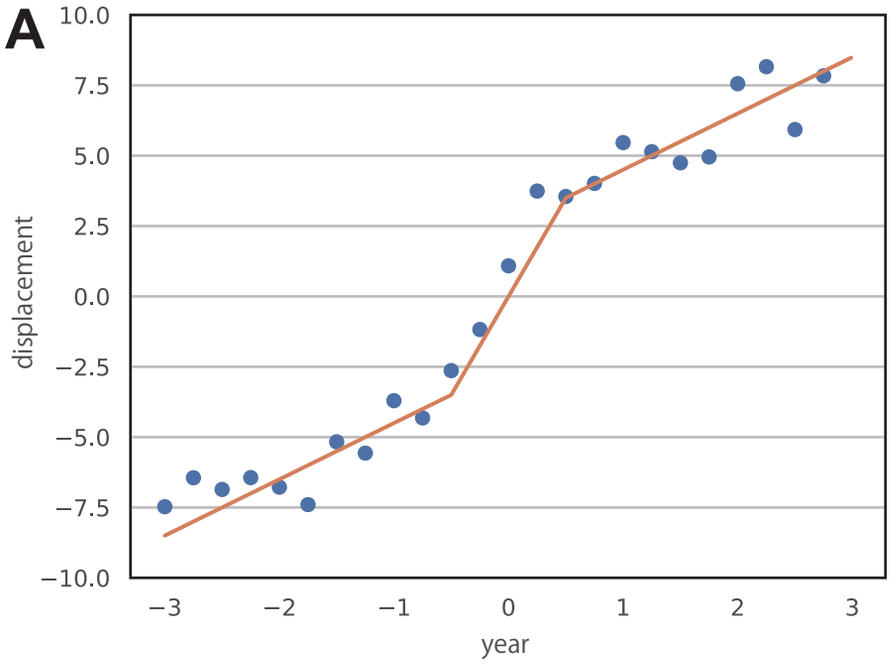
A
displacement
year

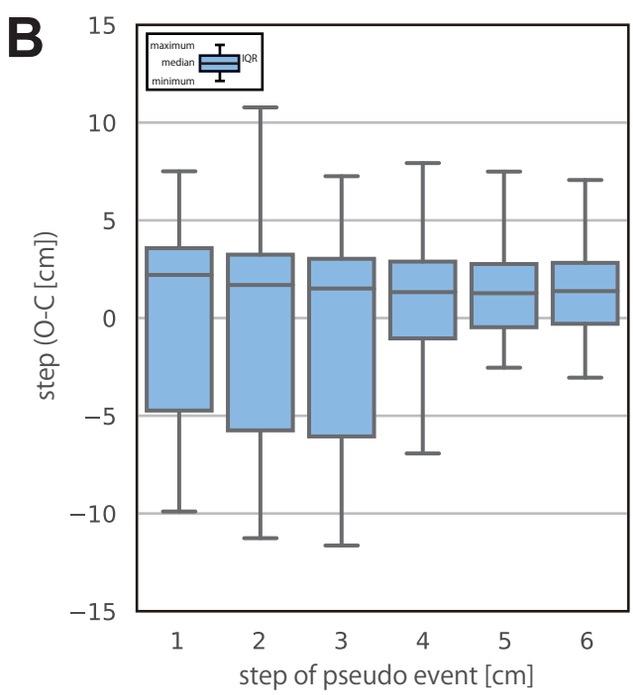
B
maximum
median
minimum
IQR
step (O-C [cm])
step of pseudo event [cm]

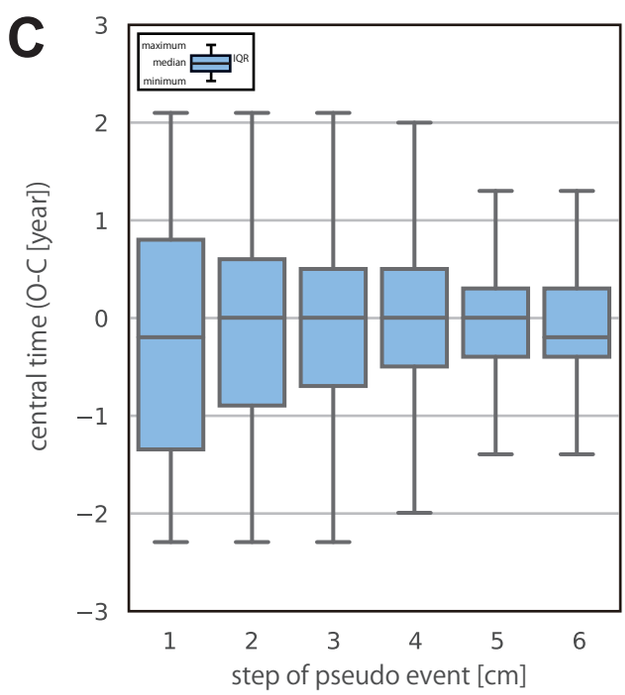
C
maximum
median
minimum
IQR
central time (O-C [year])
step of pseudo event [cm]

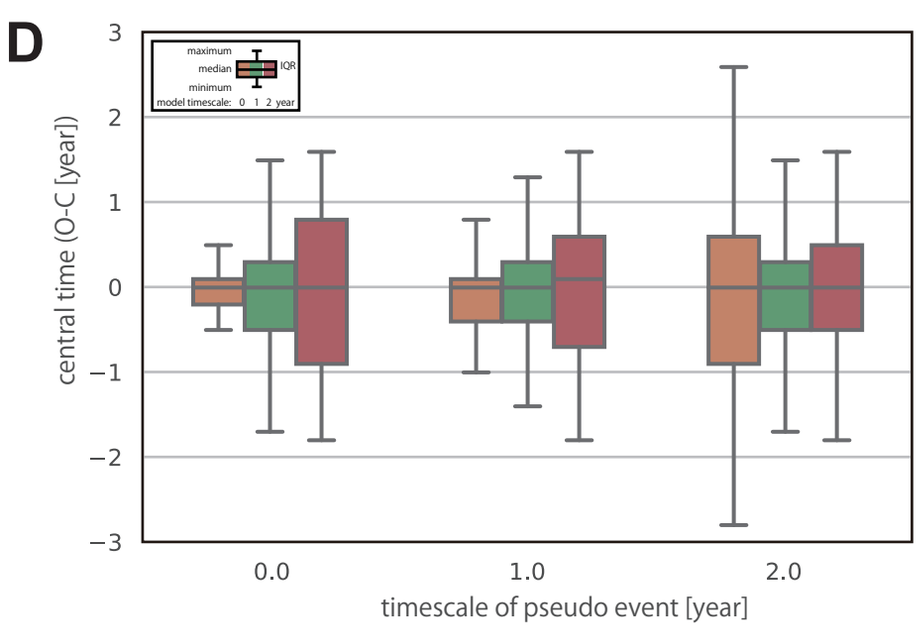
D
maximum
median
minimum
IQR
model timescale: 0 1 2 year
central time (O-C [year])
timescale of pseudo event [year]

Bungo channel

Fig S7

Onshore: 0 cm (< about 5 mm)

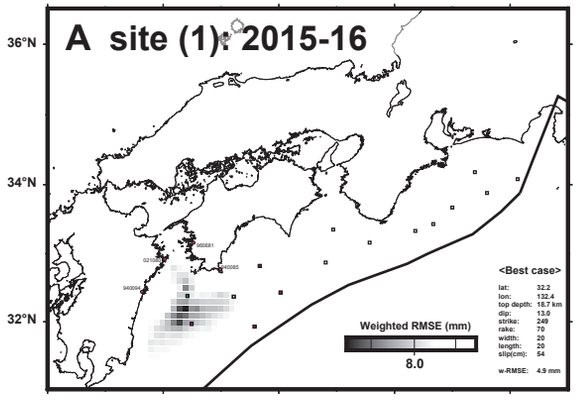

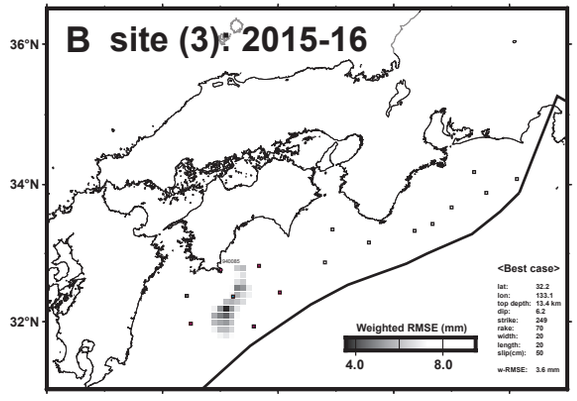

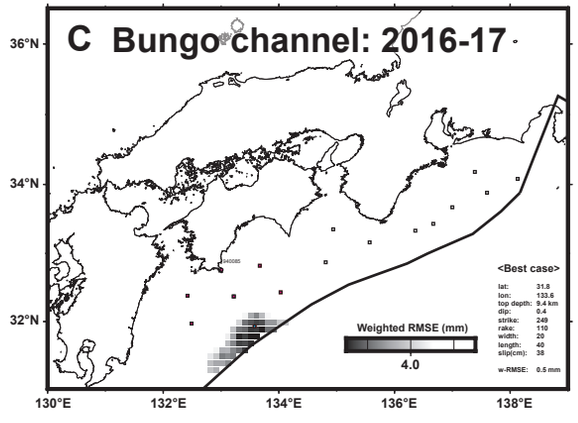

Onshore: 1 cm

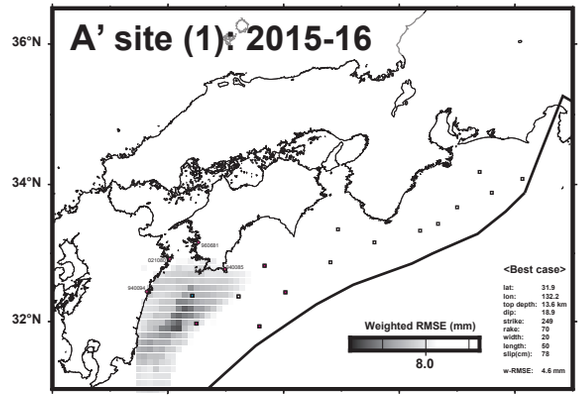

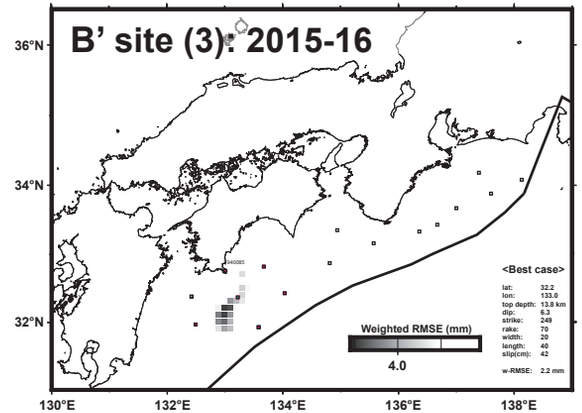

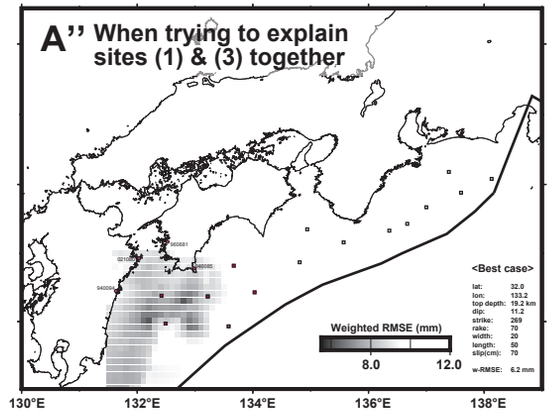

Kii channel

Fig S7

Onshore: 0 cm (< about 5 mm)

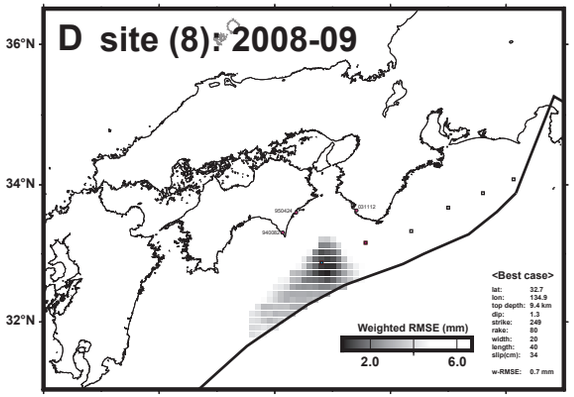

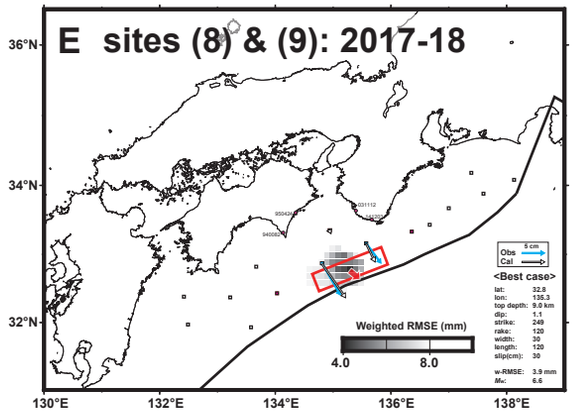

Onshore: 1 cm

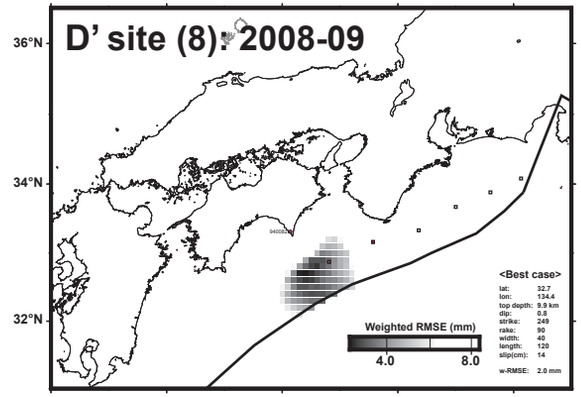

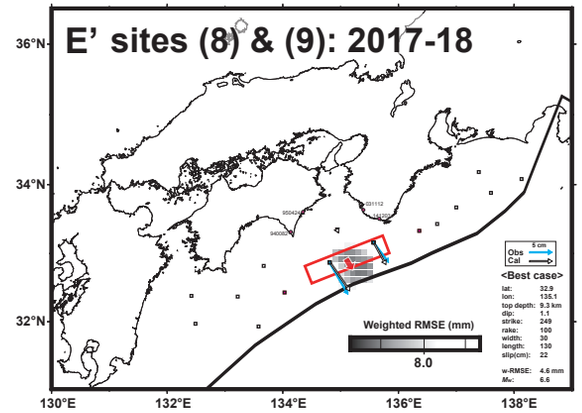

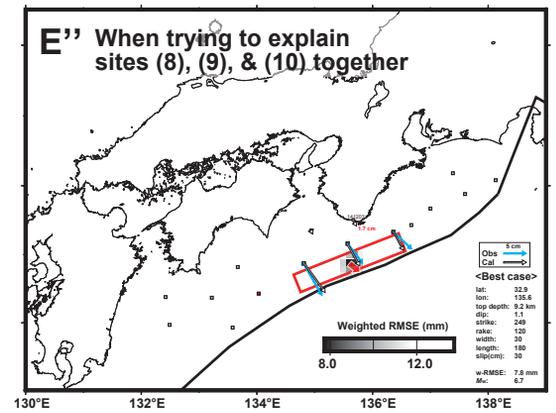

Kumano-nada

Fig S7

Onshore: 0 cm (< about 5 mm)

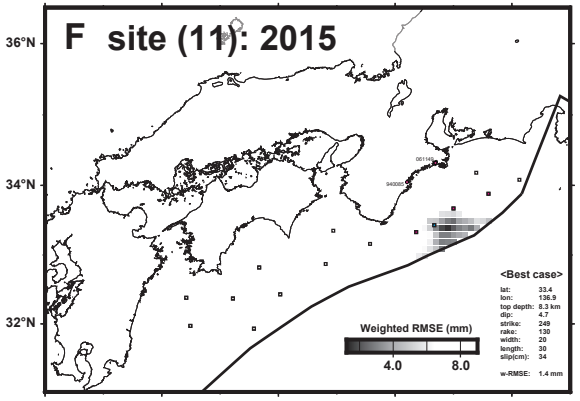

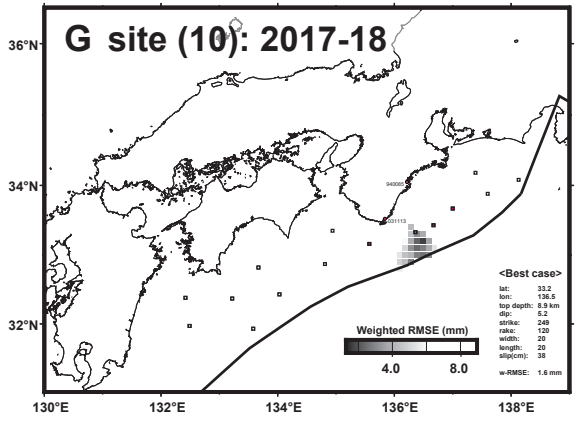

Onshore: 1 cm